

AGE-DATING ULTRALUMINOUS INFRARED GALAXIES ALONG THE MERGER SEQUENCE

T. W. MURPHY, JR.¹, B. T. SOIFER², K. MATTHEWS

Palomar Observatory, California Institute of Technology, 320-47, Pasadena, CA 91125
 tmurphy@phys.washington.edu, bts@mop.caltech.edu, kym@caltech.edu

AND

L. ARMUS

SIRTF Science Center, California Institute of Technology, 314-6, Pasadena, CA 91125
To Appear in the Astrophysical Journal

ABSTRACT

Imaging spectroscopy using the new Palomar Integral Field Spectrograph is presented for the Pa α line in four ultraluminous infrared galaxies. The resulting integral field datacubes reveal line emission possessing a wide range of complex spatial morphologies, often quite different from the appearance of the continuum. The velocity fields are equally diverse in nature, often failing to resemble typical modes of galactic motion.

We see a variety of interesting phenomena in the individual mergers including star formation rates of 2–5 M_{\odot} yr $^{-1}$ in young tidal tails; a post-encounter disk which obeys the Tully-Fisher relation; a large scale emission line nebula possibly associated with a massive outflow; an apparently single merging system possessing two distinct kinematical axes belying the presence of a second galaxy, mostly obscured by its merging companion; and possible formation of tidal dwarf galaxies.

In most cases, we are able to establish the geometry of the merger, and thus estimate the time in the merger process at which we are viewing the system. The resulting range in estimated ages, some of which are very young encounters ($\sim 5 \times 10^7$ yr), is not predicted by merger models, which produce high rates of star formation either $1-2 \times 10^8$ years after the first encounter or very late ($\sim 10^9$ yr) in the merger process. Even in the very young mergers, despite a sample selection based on extended line emission, the ultraluminous activity appears to be centrally concentrated on the nucleus of one of the progenitor galaxies—namely the galaxy with a prograde orbital geometry. The inferred extinction to these concentrations is high, usually at least 1 magnitude at the wavelength of Pa α .

The presence of a significant population of very young ultraluminous mergers, together with the majority of ultraluminous infrared galaxies existing in the final stages of merger activity, indicates that the ultraluminous galaxy phase is at least bimodal in time. An evolutionary scenario is proposed for ultraluminous infrared galaxies, wherein the far-infrared luminosity may undergo multiple ultraluminous bursts during the course of the encounter. A substantial fraction of the merger lifetime may be spent in a phase identified with the less powerful luminous infrared galaxy class.

Subject headings: galaxies: individual (IRAS 01521+5224, IRAS 10190+1322, IRAS 17574+0629, IRAS 20046–0623)—galaxies: interactions—galaxies: kinematics and dynamics—galaxies: starburst— infrared: galaxies

1. INTRODUCTION

Ultraluminous infrared galaxies (ULIRGs) are among the most luminous sources in the universe, with infrared luminosities of $L_{ir} \gtrsim 10^{12} L_{\odot}$. Imaging surveys of ULIRGs find that the vast majority of these systems are morphologically distorted, with spatial structures indicative of galactic mergers (Sanders et al. 1988; Murphy et al. 1996; Clements et al. 1996). ULIRGs are found to exist in various states of merging, from well separated galaxies to single nucleus systems that appear to have completed their nuclear coalescence. From millimeter wavelength studies of molecular gas in ULIRGs, it is found that the constituent galaxies are typically large, gas-rich spirals (Sanders, Scoville, & Soifer 1991; Downes, Solomon, & Radford 1993; Solomon et al. 1997). In general terms, the merging process destabilizes the orbits of gas within

the galaxies, leading to accumulation of gas in the central potential of the individual galaxies or merger remnant. The resulting high concentrations of molecular gas stimulate the production of stars, or in some cases fuel a massive central black hole, though both can also occur simultaneously. In addition, cloud-cloud collisions may occur within the disrupted disk, or as the galaxies begin to overlap, leading to widespread star formation. Veiled by the vast quantities of dust mixed with the molecular gas, these energetic processes are seen via dust-reprocessed light at far-infrared wavelengths, and are held to be responsible for the extreme luminosity of these systems (see Sanders & Mirabel 1996, for a review).

A new integral field spectrograph (Murphy, Matthews, & Soifer 1999) working at near-infrared wavelengths on the Palomar 200-inch Telescope has provided a new way

¹ Now at the University of Washington, Dept. of Physics, Box 351560, Seattle, WA 98195

² Also at the SIRTF Science Center, California Institute of Technology, 314-6, Pasadena, CA 91125

to probe the properties of the interstellar medium in these galaxies. Combining imaging capabilities with longslit spectroscopy, the integral field data permit simultaneous acquisition of spatial and velocity information of emission line gas over a two-dimensional region on the sky. For complex sources such as ULIRGs, the advantage over more traditional longslit or narrow-band techniques is substantial.

This paper presents the spatial and kinematic structures of the $\text{Pa}\alpha$ line emission nebulae in four ULIRGs of various morphological types. Most of the line emission observed in these galaxies is spectrally unresolved at the current resolution. Therefore, this paper concentrates on the morphologies and velocity fields of the line emission structures. The four galaxies are taken from the 2 Jy sample of Strauss et al. (1990, 1992), and are selected for their peculiar spatial and velocity structures in line emission as seen in two-dimensional near-infrared spectra taken from Murphy et al. (1999, 2001). Table 1 lists the properties of the four ULIRGs in the present sample. All cosmology-dependent calculations in this paper assume $H_0 = 75 \text{ km s}^{-1} \text{ Mpc}^{-1}$ and $q_0 = 0$.

2. OBSERVATIONS AND DATA REDUCTION

2.1. Integral Field Data

Observations were made using the Palomar Integral Field Spectrograph (PIFS) situated at the $f/70$ Cassegrain focus of the 200-inch Hale Telescope. A description of this instrument along with general observing procedures can be found in Murphy, Matthews, & Soifer (1999). In brief, the integral field spectrograph delivers simultaneous spectral information across a contiguous two-dimensional field of view with essentially seeing-limited spatial resolution in both dimensions. For these observations, the $5.4' \times 9.6'$ field of view was rotated to optimally cover the extent of the galaxies as seen in broadband infrared light, with two contiguous field positions required to cover the larger structure of IRAS 01521+5224. All observations were made in clear conditions. Table 2 provides a summary of the observations. The $R \approx 1300$ resolution mode was used to obtain spectra centered on the redshifted $\text{Pa}\alpha$ line in each galaxy. Separate sky exposures were alternated with the on-source integrations, with individual integration times of 300 s. A positional dither pattern was employed for the sequence of integrations enabling recovery of seeing-limited spatial resolution in the cross-slit direction. Observations of nearby stars for the purpose of evaluating the point spread function (PSF) accompanied the spectral observations. Wavelength calibration is provided through a combination of OH airglow lines and arc lamp spectra taken at the time of observation. Atmospheric opacity and spectral flat-fielding are compensated simultaneously using the light from a G dwarf star, spread uniformly across the field of view.

Data reduction consists of subtracting the sky integrations, interpolating static bad pixels and cosmic ray artifacts, dividing by the G star spectrum, and multiplying by a blackbody matched to the G star's temperature. Spatial and spectral distortions are then corrected using previously generated distortion maps appropriate for the particular grating setting. Co-registration of the slits in the spatial dimension is based upon observation of the G star

with its light extended perpendicular to the slit pattern by chopping the telescope secondary mirror in a triangle-wave pattern. The two-dimensional spectra from the eight slits are placed into a three-dimensional datacube according to the positional dither pattern, with a common wavelength axis established by the calibration lines. Residual OH airglow lines are removed by subtracting a scaled version of the raw sky spectrum, with typical scalings of $\sim 2\%$ in absolute value, sometimes as large as 10%. Photometric variability among individual integrations is compensated by small scaling adjustments such that the object flux is consistent from one integration to the next. A more detailed description of these general procedures may be found in Murphy, Matthews, & Soifer (1999).

In the data presented here, the pure continuum images are constructed directly from the integral field datacube, avoiding spectral regions associated with OH airglow emission or poor atmospheric transmission. For each spatial pixel, a linear fit is made to the line-free portion of the continuum spectrum. The line images are formed by subtracting this continuum fit from the datacube, then summing in the spectral dimension over a range encompassing the line emission. Because they are extracted from the same datacube, the co-registration of the continuum and line images is implicit.

The velocity fields are constructed in the following manner. At each spatial pixel, the wavelength of the peak emission is computed, and converted to a velocity. Because spatial gradients of flux across the individual slits can mimic shifts in velocity, the morphology of the line emission at the line peak is used to assess these gradients and correct the peak velocity values. These corrections are typically no larger than $30\text{--}40 \text{ km s}^{-1}$. A “maximum $\text{Pa}\alpha$ ” image is also presented for each ULIRG in order to show weaker emission with greater sensitivity. This image, also continuum subtracted, represents a single spectral resolution element centered for each spatial pixel on the wavelength of maximum line emission intensity. In other words, this image extracts spectral information only around the peak line intensity, thereby following the velocity indicated in the velocity field.

Photometric calibration was performed using the photometric system of Persson et al. (1998). Images of the standard stars were taken in the spectrograph's imaging mode through a K_s filter, and the total flux was compared to images of the science object taken in the same manner. The photometry is corrected for atmospheric opacity, and for Galactic extinction based on dust measurements by Schlegel, Finkbeiner, & Davis (1998), and using the extinction law of Rieke & Lebofsky (1985). For each of the galaxies in this sample, near-infrared spectra (e.g., Murphy et al. 2001) were available from which to judge the continuum shape, so that the continuum flux density at $\text{Pa}\alpha$ could be related to the continuum flux density in the center of the K_s bandpass. The photometric calibration was supplemented by similar procedures using the K_s imaging discussed below.

2.2. Supplementary Imaging

Continuum and narrow-band $\text{H}\alpha + [\text{N II}]$ images accompany the integral field data in Section 3, where available, in order to provide a better sense of the overall structure

of the continuum and line emission light. Most of the near-infrared images were taken through the wide-open 10 arcsecond slit of the Palomar Longslit Infrared Spectrograph (Larkin et al. 1996), operating on the 200-inch Telescope, and using a 256×256 HgCdTe array with a pixel scale of $0''.167 \text{ pixel}^{-1}$. The near-infrared image of IRAS 20046–0623 was obtained using a 58×62 InSb array camera also operating on the 200-inch Telescope with a pixel scale of $0''.313 \text{ pixel}^{-1}$. Table 3 presents the parameters of these observations, all of which used K_s filters.

Visual imaging is also presented for the four galaxies in this paper, with r band and $\text{H}\alpha + [\text{N II}]$ images obtained at the Palomar 60-inch Telescope. For IRAS 17574+0629 and IRAS 20046–0623, r band images are presented in Murphy et al. (1996), and duplicated here. The data reduction procedures for the r band images in this paper are described in Murphy et al. The $\text{H}\alpha + [\text{N II}]$ images were taken with narrow band filters ~ 10 nm wide, using the r band images as the continuum reference. Data reduction for the narrow band images is similar to that for the r band images, followed by scaling, shifting, rotating, and subtracting the r band continuum images such that nearby stars were nulled on average. The r filter bandpass does contain the $\text{H}\alpha$ light, but generally at $\lesssim 10\%$ of the total flux. Photometric calibration was accomplished by use of the spectrophotometric standards from Oke & Gunn (1983), correcting for atmospheric opacity, and for Galactic extinction by the same methods described at the end of Section 2.1. Table 4 presents a summary of the visual observations. No $\text{H}\alpha$ data exist for IRAS 10190+1322, and the r band image for this galaxy was taken through clouds with the telescope unguided.

3. INDIVIDUAL OBJECTS

3.1. IRAS 01521+5224

3.1.1. Morphology of Continuum & Line Emission

IRAS 01521+5224 is a morphologically complex galaxy consisting of two primary galaxies and many clumps of distributed tidal debris. The two nuclei are separated by $5''.5$ (7.6 kpc projected separation) at a position angle of 25° , as determined from the near-infrared image. Near-infrared spectra of this galaxy appear typical of starburst-dominated ULIRGs (Murphy et al. 2001). Figure 1 shows both a K_s band image and an r band image of the galaxy, along with an image in $\text{H}\alpha + [\text{N II}]$. The nature of the lower surface brightness features is not immediately clear from these images. These features could be tidal tails, small companion galaxies, or fragments of the primary galaxies. The r band image demonstrates that the high surface brightness features are contained within a relatively small region. In other words, there is no obvious tidal tail component extending away from the main concentration of light at the current level of image depth. Comparing to simulations of galaxy mergers (e.g., Mihos & Hernquist 1996; Barnes & Hernquist 1996), one finds a similarity between this morphologically complex system and those model systems as seen shortly after the first close encounter. Note the absence of a distinct southern nucleus in the r band image, in contrast to the appearance of a well defined nucleus in the K_s image. The $\text{H}\alpha + [\text{N II}]$ image, which has a dramatically different morphology from

the continuum emission, is discussed in relation to the $\text{Pa}\alpha$ images in Section 3.1.2.

Figure 2 presents the PIFS data of IRAS 01521+5224, showing images of the pure continuum, total $\text{Pa}\alpha$ line emission, maximum $\text{Pa}\alpha$ emission, and the velocity field of the $\text{Pa}\alpha$ emission peak. The large extent of this galaxy required observations in two adjacent and contiguous fields, the positions of which are indicated in Figure 1. The $\text{Pa}\alpha$ emission distribution is markedly different from that of the continuum light. The $\text{Pa}\alpha$ peak is coincident with the southern galaxy continuum peak, though it is not symmetrically distributed about the continuum peak position. The northern galaxy nucleus has very little $\text{Pa}\alpha$ emission associated with it, identifying the southern nucleus as the primary source of star formation, and thus presumably of the far-infrared emission.

The off-nuclear $\text{Pa}\alpha$ emission is extended over an impressive 15 kpc, mostly arranged in clumps along a ring-like structure—much like that seen in the $\text{H}\alpha$ image. Combined with the velocity information provided in the integral field datacube, the morphology of these features enables one to develop a model for the current merger geometry of the system, as will be discussed in Section 3.1.3.

3.1.2. Extinction & Star Formation

Using the $\text{H}\alpha$ image together with the $\text{Pa}\alpha$ image, one may compute line ratios to derive measures of the extinction to the various regions in the galaxy. The total $\text{Pa}\alpha$ flux within the PIFS field is $\gtrsim 2.1 \times 10^{-17} \text{ W m}^{-2}$, compared to $1.3 \times 10^{-16} \text{ W m}^{-2}$ for $\text{H}\alpha + [\text{N II}]$ in a similar aperture. Assuming an intrinsic $\text{H}\alpha/\text{Pa}\alpha$ line ratio of 8.6 (Osterbrock 1989, Case B, $n_e = 10^4 \text{ cm}^{-3}$, $T = 10000 \text{ K}$), a lower limit can be placed on the average extinction to the source of $A_V > 0.5 \text{ mag}$. The extinction at $\text{Pa}\alpha$ is interpolated from the extinction law of Rieke & Lebofsky (1985), with $A_{\text{Pa}\alpha} = 0.145 A_V$. This and all other extinction measures in this paper assume no contribution from $[\text{N II}]$, which is often half the strength of $\text{H}\alpha$ in star forming regions. Including a flux contribution from $[\text{N II}]$ at this level adds another half-magnitude to the estimated visual extinction. As such, all extinction values are stated as lower limits. The southern nucleus itself contributes 30% of the total $\text{Pa}\alpha$ flux, though a quick inspection of Figure 1 shows that the $\text{H}\alpha$ flux from this nucleus contributes a much smaller fraction of the total $\text{H}\alpha$ line emission. The extinction to the southern nucleus line emission measures $A_V \gtrsim 2.5 \text{ mag}$. Away from the southern nucleus, the visual extinction is typically 0–0.75 mag.

The hydrogen recombination flux can be used to calculate the star formation rate (SFR) in the galaxy, following the prescription for converting $\text{H}\alpha$ flux to the global SFR outlined in Kennicutt (1983). The $\text{Pa}\alpha$ line is used rather than the $\text{H}\alpha$ line, as it suffers much less from extinction. An extinction-corrected $\text{H}\alpha$ flux, used in calculating the SFR, is inferred from the $\text{Pa}\alpha$ flux using an intrinsic line ratio of 8.6, as introduced above. The $\text{Pa}\alpha$ flux is itself uncorrected for extinction, such that the SFR estimate performed in this manner represents a lower limit. For the total $\text{Pa}\alpha$ emission recorded in the PIFS field, the SFR is computed to be $\gtrsim 20 M_\odot \text{ yr}^{-1}$. As suggested above, the southern nucleus is responsible for about 30% of this total, with the rest split between the isolated clumps seen

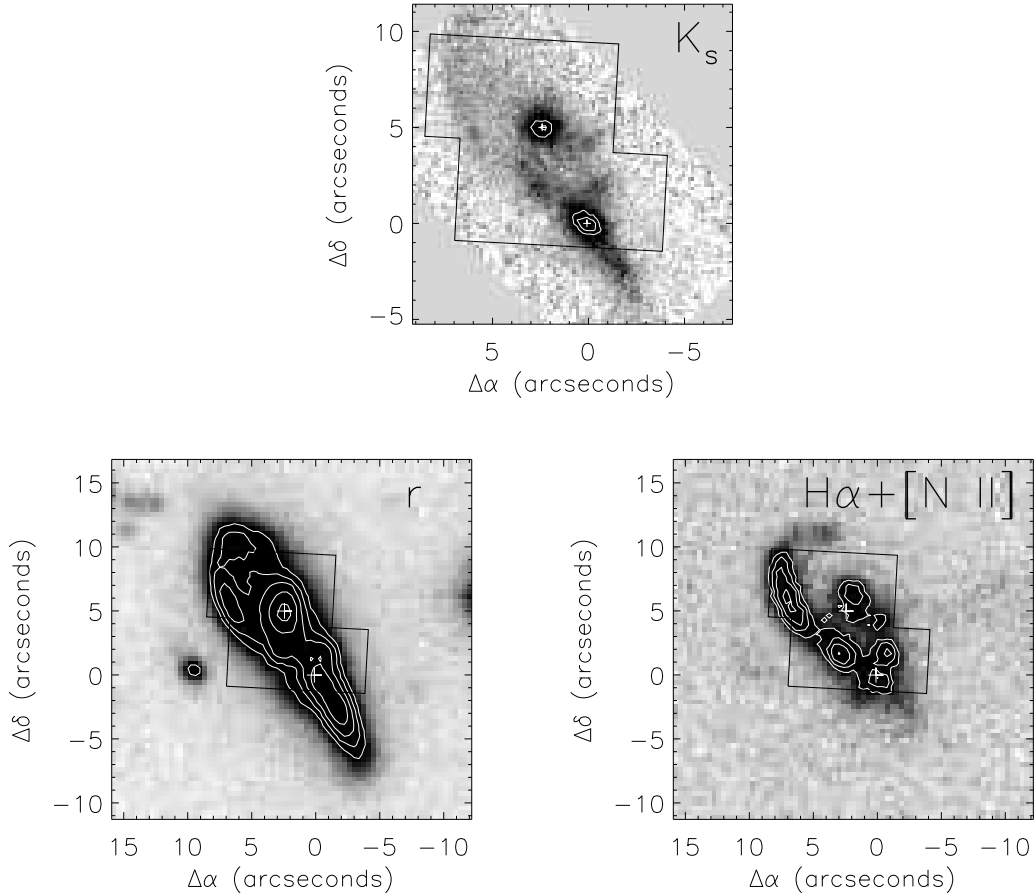


FIG. 1.— Continuum images of IRAS 01521+5224 in K_s (top) and r (lower-left) bands. These images portray a dramatically disturbed ULIRG, with four r band peaks visible, two of which are the obvious nuclei in the infrared image. Note the lack of any major features extending beyond the main grouping. A narrow band image in $H\alpha + [N\ II]$ is presented at right, showing many emission peaks arranged along a ring-like structure. The irregular box outline shows the region observed with the integral field spectrograph. Crosses indicate the positions of the near-infrared continuum peaks. North is up, and east to the left.

in Figure 2.

A surprisingly large amount of star formation appears to be occurring in isolated clumps distributed along what are thought to be tidal tails—discussed at length below. Tidal tails generally do contain gas, as they are composed of material rather indiscriminately pulled from a contiguous region of the parent galaxy, within which stars and gas are mixed with similar global distributions. Star formation is known to occur in tidal tails (e.g., Chomey et al. 1998), and tails are, in fact, seen to contain many young, blue stars (Tyson et al. 1998; Reshetnikov 1998). The star formation rate estimated for the bright $Pa\alpha$ clump in the northeast tail is $\sim 6 M_\odot \text{ yr}^{-1}$, which is unusually high for such environments (Hibbard & van Gorkom 1996; Duc & Mirabel 1998; Duc et al. 2000). Typical star formation rates in tidal clumps and tidal dwarf galaxies are estimated at $0.05\text{--}0.2 M_\odot \text{ yr}^{-1}$. The highest previously observed star formation rates in tidal tails also occurs in ULIRGs, with about $0.5 M_\odot \text{ yr}^{-1}$ (Mihos & Bothun 1998). The very high rate of star formation in the clump may be the result of gas compression induced by crossing orbits in the forming tail. The work by Toomre & Toomre (1972) points out that shortly after tidal tails develop, the tidal material on the inside of the tail overtakes the outer material. The crossing orbits that result compress the gas within the

tail, leading to heightened star formation—at least in low inclination systems (Wallin 1990). This scenario, which is relevant only for very young tails, is consistent with the estimated age and geometry of the IRAS 01521+5224 encounter, as discussed below.

3.1.3. Merger Geometry

The complex morphology of the IRAS 01521+5224 merger does not lead to an immediate understanding of the merger state of this galaxy pair. At first glance, the $H\alpha$ and $Pa\alpha$ emission appears to be distributed around an elliptical ring, roughly centered on the northern galaxy nucleus. Though rings of comparable size and star formation activity have been observed in galaxies like the Cartwheel (Higdon 1995) and AM 0644–741 (Higdon & Wallin 1997), we favor an interpretation that naturally accounts for the various observed properties by way of tidal tails. We briefly discuss the ring interpretation before presenting the tidal tail model. A more complete discussion of the observations supporting the merger model presented below can be found in Murphy (2000).

Arguments for a ring include the approximate elliptical shape of the line emission, and the location of the northern galaxy near the center of the ellipse. If the material within the ring is orbiting the central galaxy, the maximum projected radial velocities will be observed at

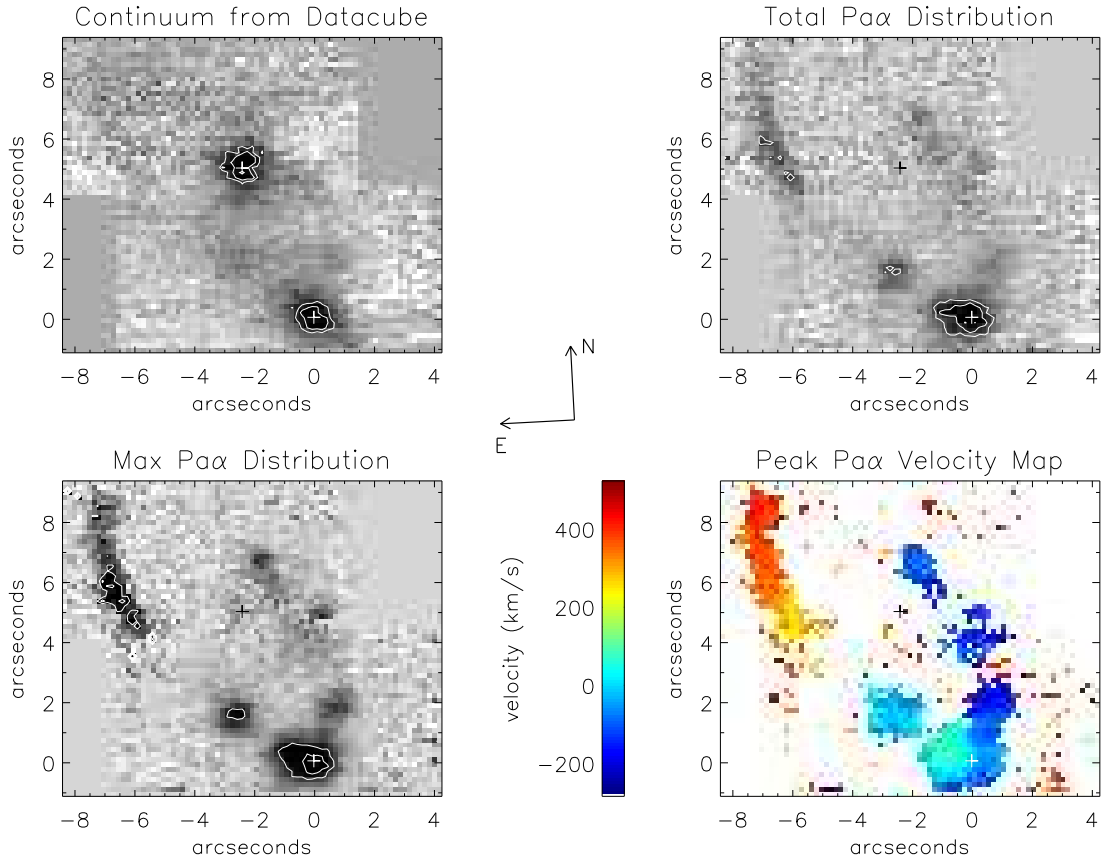


FIG. 2.— PIFS data on the central region of IRAS 01521+5224. At top left is the line-free continuum image reconstructed from the datacube. At top right is the total $\text{Pa}\alpha$ emission, continuum subtracted, and summed from -325 to $+480$ km s^{-1} relative to the systemic velocity. A higher contrast $\text{Pa}\alpha$ image, tracing the peak $\text{Pa}\alpha$ emission as described in the text, is shown at lower left. Finally, the velocity field is represented at lower right as a color diagram, with red representing redshifted gas, and blue representing blueshifted gas. The velocity scale is indicated to the left of the plot. In all images, the continuum peak locations are indicated by crosses. Field orientation is indicated by the arrows, with “left” corresponding to a position angle of 87° .

either end of the ellipse—much like what we see in Figure 2. Figure 3 shows a position-velocity plot constructed along a spatial loop following the $\text{Pa}\alpha$ line emission. From this it is seen that there is little or no change in velocity along the western part of the ellipse, arguing against the ring interpretation. Moreover, the velocity mismatch of ~ 200 km s^{-1} across the minor axis of the ellipse is unexplained by the rotating ring model, since this model predicts identical velocities across the ring’s projected minor axis. This mismatch could be explained in part by a radial expansion of the rotating ring (e.g., Higdon, Rand, & Lord 1997). However, the asymmetry in the velocity profile around the ellipse—most notably the monotonic western portion—remains problematic. Both the ring and tidal tail models for IRAS 01521+5224 require special viewing angles leading to coincidental projections, projecting the southern nucleus either onto the ring or onto the tail from the northern galaxy.

We favor the tidal tail model over the ring model, in part because tails are ubiquitous features of merging systems, while rings are far less common, requiring a carefully arranged encounter—often with the disturbing galaxy passing through the central region of the ringed galaxy from a polar direction. Figure 4 is a schematic representation of our view on IRAS 01521+5224 in the context of our model of the merger geometry. The orientation follows

that in Figure 1. In this model, the southern galaxy is in the background, seen nearly edge-on. Thus the elongated structure in the K_s image at a position angle near 45° and symmetrically located with respect to the southern nucleus represents the disk of the southern galaxy. The edge-on appearance is also suggested by the high nuclear extinction to the southern nucleus—both in line emission and continuum light. The arcing feature to the east and north—as seen in line emission—is a tidal tail connecting to the back side of the southern galaxy disk plane. The northern galaxy, viewed more nearly face-on, has a tenuous tail to the west that is by chance projected onto the vicinity of the southern galaxy nucleus. Figure 5 shows what this pair of galaxies might look like from a vantage point directly over the orbital plane. The geometry proposed for the southern galaxy closely resembles that seen following the first encounter in many numerical merger models containing prograde disks (see especially Mihos & Hernquist 1996, Fig. 13).

The senses of rotation depicted in Figures 4 and 5 are derived from the $\text{Pa}\alpha$ velocity field. Though the velocity field in Figure 2 does not yield information on the radial velocity or rotation state of the northern nucleus, two-dimensional spectral extractions from the datacube, shown in Figure 6, provide enough information to determine that the northern galaxy is blueshifted relative to the southern

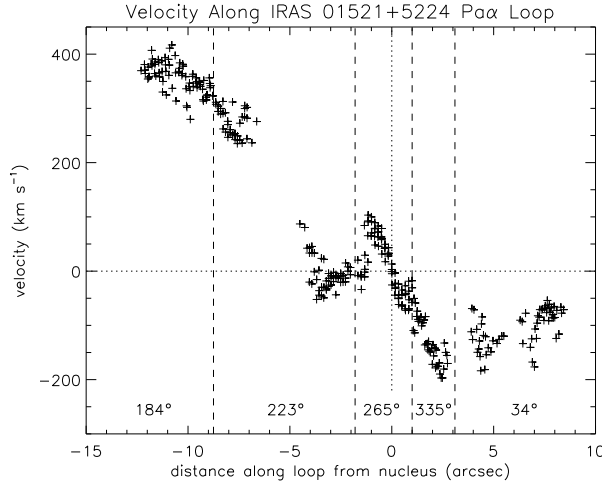


FIG. 3.— Segmented position-velocity plot along the loop of Pa α emission in IRAS 01521+5224, starting in the northeast, and winding around in a counter-clockwise sense, through the southern continuum peak, then back to the north. The loop was broken into five straight-line segments, with breakpoints and position angles represented on the plot, delineated by dashed lines. The displacement is plotted as accumulated linear distance along the segments. The southern nucleus is at the zero position on the horizontal axis, displaying a rotation curve with an amplitude of about 150 km s^{-1} . Note the fast moving clump at upper left (northeast clump), with a velocity gradient projecting directly away from the southern nucleus center. This clump was broken into two linear slit segments owing to its spatially curved nature.

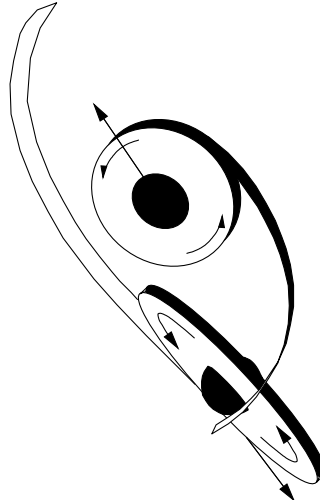


FIG. 4.— A schematic model of the IRAS 01521+5224 system, as seen from our viewpoint. The northern (upper) galaxy, nearly face-on, is in the foreground of the southern galaxy, which is seen nearly edge-on. The eastern tail spins off of the southern galaxy, and is seen in almost pure recession. The western tail, extending from the northern galaxy, is almost in the plane of the sky, explaining the very small observed velocity gradient along this tail. Bulges are placed in the diagram to approximate the appearance of the K_s image in Figure 1.

galaxy by $\sim 50 \text{ km s}^{-1}$, and that it is weakly rotating at a position angle between 45° and 90° . An arrangement such as that shown in Figure 5 is consistent with the morphologies and velocity fields observed in IRAS 01521+5224, with our view restricted to the shaded region, and very likely from a vantage close to the orbital plane. The northern galaxy in this figure is not accurately represented, and should be rotated out of the plane of the paper in order to more closely match the observations.

The proposed geometry, along with the presumed vantage point from near the orbital plane, means that the southern galaxy's rotation plane is nearly coincident with the orbital plane, in a highly prograde configuration. The northern galaxy is then inclined with respect to the orbital plane, itself being weakly prograde (see Toomre & Toomre 1972, for definitions of prograde and retrograde).

The following observations lend support to the tidal tail

interpretation. The eastern tail very naturally interfaces with the southern galaxy disk plane, both in terms of position angle on the sky and the velocity field, which matches the rotation sense of the southern galaxy. The western tail also joins the northern nucleus, seamlessly tying into its velocity field, as indicated in Figure 6. The nearly constant velocity of the western tail is consistent with the deduction that we view the northern galaxy nearly face-on, such that the tail—moving primarily in the rotation plane of its parent galaxy (Toomre & Toomre 1972)—has little motion along our line-of-sight. Though the H α morphology is rather closely elliptical in shape, there is a slight departure at the northern end of the eastern tail. While it is true that the western tail coincidentally terminates on both the northern and southern galaxies, the H α image hints that the tail may slightly overshoot the southern nucleus, as reflected in Figure 4.

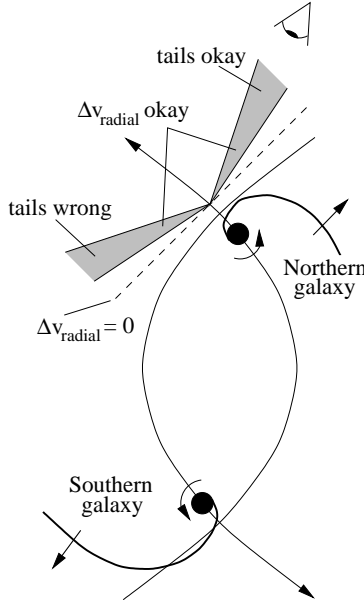


FIG. 5.— Schematic diagram of the likely orbital plane geometry of the IRAS 01521+5224 merger, indicating probable locations of our vantage point. The dashed line represents a plane from which the galaxies would currently show no relative radial velocity. The shaded grey region, when revolved about the current relative velocity vector, represents the region of space from which the northern galaxy is slightly blueshifted relative to the southern galaxy. Only from the upper right portion of this region do the tidal tails have the correct observed velocities.

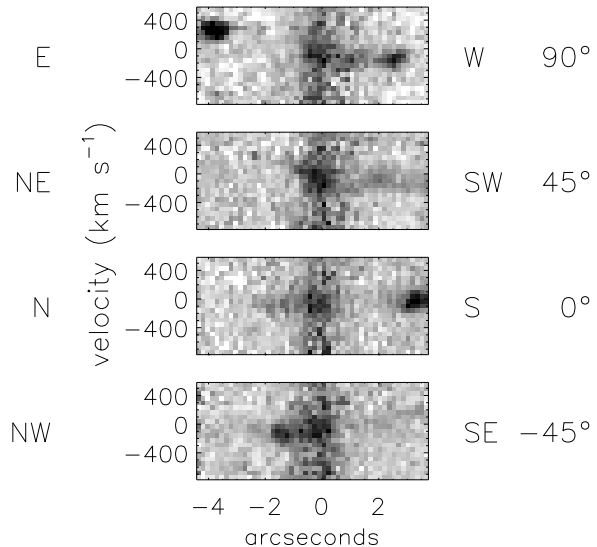


FIG. 6.— Four two-dimensional spectra of the northern nucleus extracted from the IRAS 01521+5224 datacube corresponding to four slits at position angles of 90° , 45° , 0° , and -45° show that there is $\text{Pa}\alpha$ emission associated with this nucleus. The vertical scale is in km s^{-1} relative to the southern nucleus velocity. The continuum from the nucleus can be seen in the center of each spectrum, with line emission appearing at about -50 km s^{-1} . A slight rotational motion is inferred from the apparent tilts of the line emission, with the maximum gradient probably at a position angle between 45° and 90° . The emission from the western tail is seen to smoothly interface with the nuclear emission, seen most clearly in the top panel.

Having adopted the tidal tail interpretation of the IRAS 01521+5224 morphology, a few other circumstances fall neatly into place. The geometry of the model, as portrayed in Figure 5, shows that the two galaxies have just passed a close encounter. This explains the impressive level of complexity seen in IRAS 01521+5224, and accounts for the short, high-surface-brightness appearance of the newly formed tails. In the same vein, the very high rate of star formation in the tails can be understood in terms of gas compression resulting from crossing orbits in

young tails (Toomre & Toomre 1972; Wallin 1990). This compression is relevant only for low inclination systems, as we believe the southern nucleus in IRAS 01521+5224 to be. The highly prograde geometry of the southern galaxy not only explains the prompt formation of a tidal tail, but also may explain *why* this galaxy is ultraluminous. Prograde galaxies are highly susceptible to the formation of bar potentials around the nucleus, so that they are very effective at funneling gas into high concentrations in the central regions of the galaxy. It is this fast-acting response

that enables IRAS 01521+5224 to appear ultraluminous at this early stage of merging. This topic is discussed at greater length in Section 4.

3.1.4. Age of Merger

The current position and velocity of the tidal tails can be used to estimate a merger age for IRAS 01521+5224. The elongated Pa α feature in the northeastern corner of the field is appreciably redshifted relative to the southern nucleus. This clump (hereafter the northeast clump) appears to lie in the tidal tail originating from the southern galaxy. The clump's velocity gradient, seen in Figure 3, points directly at the plot origin, corresponding to the position-velocity of the southern nucleus. Such an arrangement in position-velocity space would be expected in a very simplified model of tidal tail production, wherein a mass of material is extracted from a single location in the source at an instant in time. In such a scenario, the faster moving mass moves farther away in the same amount of time. In reality, tidal tails are not formed instantly, and the constituent mass is pulled out of a zone in the galaxy, rather than a single point. Yet overall, the simulations of tidal tail formation by Toomre & Toomre (1972) are in agreement with this generic velocity profile.

The physical distance between the southern nucleus and the middle of the northeast tidal clump is around 15 kpc, based on the geometrical projections surmised from the geometry developed in Section 3.1.3. This distance is traveled in 5×10^7 yr at the measured recessional speed of 300 km s $^{-1}$, which is roughly consistent with the estimated timescale for the formation of such structures in the galactic merger models (e.g., Barnes & Hernquist 1996; Mihos & Hernquist 1996, see in particular panel 3 of Fig. 13). It was mentioned previously that the high rate of star formation in young tidal tails is consistent with the formation of caustics (i.e., crossing orbits) as found in simulations of tidal disturbances. Wallin (1990) showed that the caustic within a tidal tail starts at the root of the tail and travels outward along the tail. This provides a natural explanation for the detachment of the intense star formation region from the main body of the southern galaxy, and can also be used to compare the development stage of the IRAS 01521+5224 merger with that of merger simulations.

One may speculate that the northeastern tidal clump, with its high velocity and high rate of star formation, may evolve into a detached, blue galaxy with properties typical of dwarf galaxies. If the clump is not tidally stable, this single feature could give rise to multiple dwarf galaxies. The notion that dwarf galaxies can be spawned in tidal tails was originally proposed by Zwicky (1956). Schweizer (1978) found observational evidence for this conjecture at the tip of the southern tidal tail in the Antennae (NGC 4038/9). More recent observations (Mirabel, Dotto, & Lutz 1992; Hibbard & van Gorkom 1996; Duc & Mirabel 1998) have found additional evidence for the tidal clump/dwarf galaxy connection. Simulations verify the plausibility of self-gravitating conglomerates with masses similar to those of dwarf galaxies forming out of tidal tail material (Barnes & Hernquist 1992; Elmegreen, Kaufman, & Thomasson 1993). The clump is almost certainly tidally unstable, given its proximity to the parent galaxies and very large velocity gradient. It is not clear that even the

outermost, fastest-moving material has enough velocity to escape the system. Even if ultimately bound, this knot of material could develop into a number of self-gravitating systems in very long-lived orbits about the center of mass of the post-merger galaxy system. More detail on the dynamical properties of the northeastern tidal clump can be found in Murphy (2000).

3.2. IRAS 10190+1322

3.2.1. Morphology of Continuum & Line Emission

IRAS 10190+1322 is a double-nucleus ULIRG with a projected nuclear separation of 4''.0 (5.3 kpc) along a position angle of 65°, and characterized as an H II galaxy by the visual spectrum of Veilleux, Kim, & Sanders (1999). Figure 7 shows the appearance of the continuum emission for the merging system. The *r* band image is of poor quality, and is included only to highlight the differing continuum flux ratio between nuclei in the visual and infrared bands. In the K_s image, the eastern galaxy appears more concentrated than the western galaxy, which shows diffuse emission surrounding the nucleus. While the nuclear components have a 1.6:1 flux ratio in 1''.5 box apertures, the eastern nucleus being brighter, the total continuum fluxes in larger apertures of the companion galaxies approach the same value. Each galaxy measures $K_s \approx 13.05$ mag in 4'' \times 5'' and 5'' \times 5'' apertures for the eastern and western galaxies, respectively. The *r* band ratio, by contrast, is 0.7:1 in similar apertures.

Figure 8 shows the appearance of the Pa α emission across this system. The Pa α emission is distributed similarly to the continuum emission, with a compact eastern source and a diffuse nebula surrounding the central peak of the western source. The ratio of Pa α fluxes in small apertures around the nuclear concentrations is 3.2:1, while the total Pa α flux for the two galaxies is roughly the same, indicating that the line emission is much more diffuse in the western galaxy than in the eastern galaxy. The off-nucleus line emission in the western galaxy is fairly uniform across its large extent, except for a knot of emission between the two nuclei. It is worth noting that a longslit spectrum of this pair of galaxies would have missed the bulk of the line flux in the western galaxy, leading one to potentially mis-judge the relative importance of star formation in these two galaxies.

3.2.2. Star Formation & Extinction

Converting the total Pa α flux in the PIFS field of 2.9×10^{-17} W m $^{-2}$ into a star formation rate, as described in Section 3.1.2, yields a total system SFR of $27 M_{\odot}$ yr $^{-1}$, split rather evenly between eastern and western galaxies. The clump of line emission between the two galaxies hosts approximately $1-1.5 M_{\odot}$ yr $^{-1}$ of star formation. Most of the star formation is likely buried in the eastern nucleus, as judging by the 6 cm radio continuum from Crawford et al. (1996). The radio map has resolution of 4'', coinciding with the separation of the two nuclei. The radio contours, peaking on the eastern nucleus, are stretched out toward the direction of the western nucleus. It is obvious that the eastern nucleus dominates the radio emission. The ratio of radio emission to far-infrared emission in IRAS 10190+1322 is much like that of other starburst galaxies, with a $q \equiv \log(S_{FIR}/S_{20\text{cm}})$ parameter of 2.38,

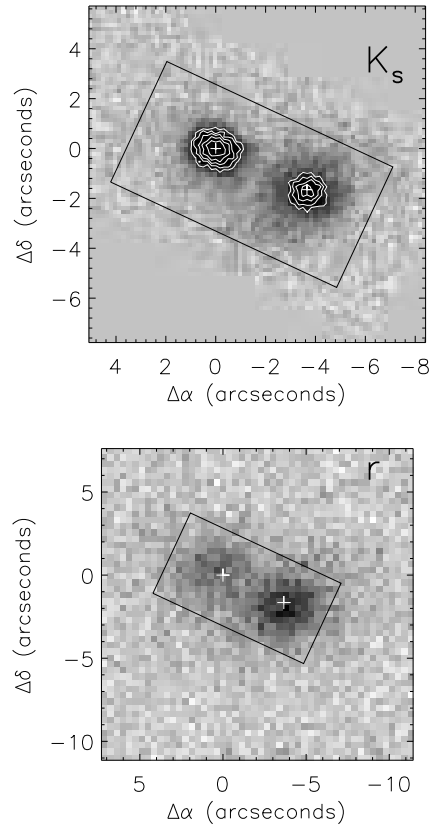


FIG. 7.— Continuum images of IRAS 1019+1322 in the K_s and r bands. The r band image was obtained in adverse conditions, preventing a meaningful investigation of large scale tidal debris. Note the reversal of the dominant nucleus between the visible and infrared images. The PIFS field is represented as a rectangular outline in both images. Crosses indicate the positions of the near-infrared continuum peaks. North is up, and east is to the left.

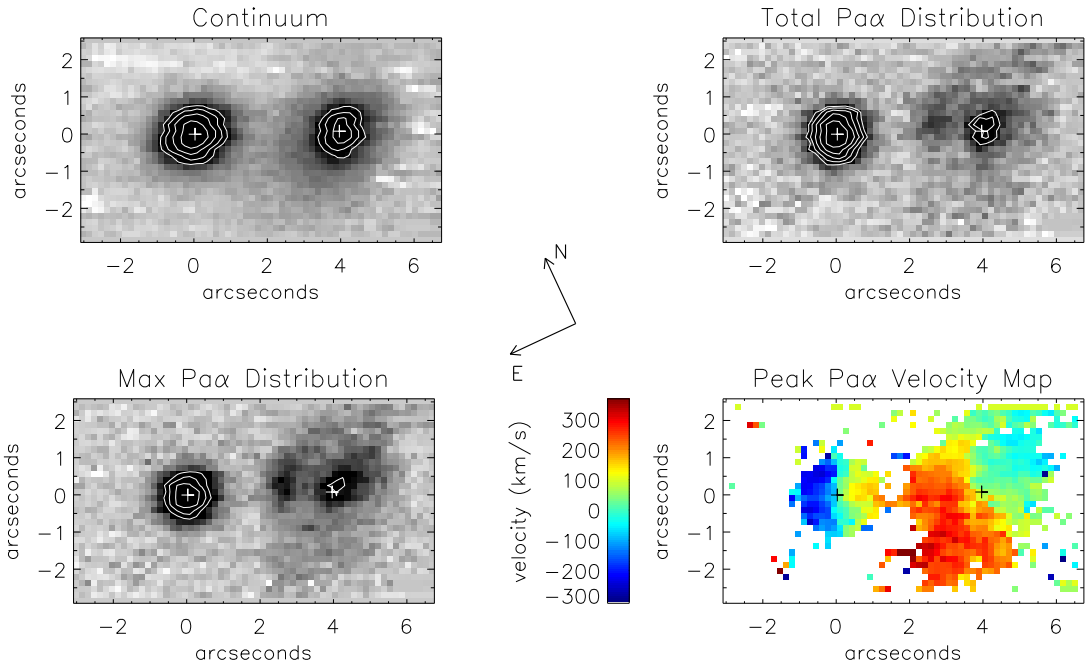


FIG. 8.— Integral field data for IRAS 10190+1322. Description of the four images follows from the Figure 2 caption. Crosses coincide with the positions of the continuum peaks. The field orientation is as indicated by the arrows, with “left” corresponding to a position angle of 65° .

compared to the average starburst $q = 2.40 \pm 0.26$ as reported by Crawford et al..

Under the assumption that the radio emission traces

star formation, and that Pa α does the same, though subject to greater extinction, one may estimate the amount of star forming activity hidden from view at $2\ \mu\text{m}$ in the

eastern nucleus. Gaussian smoothing the $\text{Pa}\alpha$ emission map to a resolution of $4''$, after artificially adjusting the flux ratio of the eastern and western contributions, one finds that the radio map is consistent with a 2.5:1 flux ratio between the two components. Another way to put this is that the eastern galaxy's $\text{Pa}\alpha$ emission on average suffers one magnitude more extinction than does the $\text{Pa}\alpha$ emission in the western galaxy. Though no extinction estimate is available from $\text{H}\alpha$ measurements, the foregoing estimate would result in a visual extinction around 7 mag. An extinction estimate based on an actual measurement of the $\text{H}\alpha$ flux would almost certainly be less than this since the dust is probably mixed with the line emission source, so that the $\text{Pa}\alpha$ light is incapable of probing to the center of the obscuration.

Using the extinction estimated via the 6 cm map to adjust the above star formation rate estimate, the total SFR is closer to $50 M_\odot \text{ yr}^{-1}$, with much of this obscured by heavy dust extinction in the eastern nucleus. This is still probably a lower limit to the star formation in the two galaxies, as extinction common to both galaxies is not taken into account. A rough estimate of the unaccounted star formation may be established by the expectation from Scoville & Young (1983) that the star formation rate will be greater than $\sim 75 M_\odot \text{ yr}^{-1}$ for a galaxy with a bolometric luminosity of $10^{12} L_\odot$.

3.2.3. Merger Geometry & Age

Unlike the other ULIRGs in this sample, IRAS 10190+1322 exhibits a rather organized kinematical state—that of simple rotation of the two components, as seen in Figure 8. The knot of $\text{Pa}\alpha$ between the two nuclei does not stand out in the velocity map, showing that it is simply a local hot-spot in the disk of the western galaxy, and not a separate kinematical component. Rotation curves for each of these two galaxies are presented in Figure 9. The eastern galaxy has a total velocity amplitude of around 350 km s^{-1} , and the more extended western galaxy shows a 340 km s^{-1} velocity amplitude. The centers of these galaxies are moving at a relative velocity of $\sim 110 \text{ km s}^{-1}$, with the eastern galaxy blueshifted relative to the western galaxy. This configuration in velocity space suggests that the eastern galaxy is in a prograde configuration, while the western galaxy is retrograde.

The extent of the $\text{Pa}\alpha$ emission in the western galaxy, as visible in Figure 8, is an impressive seven kpc across. The morphology is suggestive of a disk inclined at about 40° – 50° , in which case the deprojected maximum velocity difference along the major axis implies a circular velocity full amplitude of 450 – 530 km s^{-1} . This value is consistent with the expectation from the H band Tully-Fisher relation (Pierce & Tully 1992) based on the broad-band absolute magnitude of the western galaxy ($K_s = 13.0$ mag; $M_{K_s} = -24.6$ mag; $\Delta v \approx 530 \text{ km s}^{-1}$, assuming $H - K \approx 0.8$ for ULIRGs, as in Carico et al. (1990)). Though it would seem that galaxies having endured a close encounter would not be able to maintain a rotation profile in agreement with the Tully-Fisher relation—as observed in the western galaxy—it is found that even rather disturbed disks do not lie far from this relationship (Mihos & Bothun 1997; Barton et al. 2001).

If indeed the eastern galaxy is prograde and the western

galaxy is retrograde, the fact that the eastern galaxy is more compact in $\text{Pa}\alpha$ than is the western galaxy, and additionally is the site of the most intense star formation, is in excellent agreement with expectations of gas concentrations based on encounter geometry. A galaxy in a prograde configuration experiences near resonance with the orbital motion of the companion, leading to exaggerated tidal disturbances. These disturbances often manifest themselves in the form of bar modes in the galactic disks, which serve to torque and funnel gas from the disk to the central regions of the galaxy (Mihos & Hernquist 1996), creating a compact central gas concentration. Retrograde encounters, on the other hand, are far less disruptive (see Toomre & Toomre 1972), such that the disk is not significantly disturbed owing to an averaging out of tidal forces from the companion. Therefore, retrograde disks do not experience appreciable nuclear gas concentrations following the initial encounter. The match to the observational data for IRAS 10190+1322 is reassuring, and helps strengthen our identification of the eastern galaxy as prograde and the western galaxy as retrograde.

Despite the fact that the majority of the infrared luminosity can be associated with the eastern, prograde galaxy, the western galaxy nonetheless is hosting substantial star formation activity. With an estimated SFR of at least $13 M_\odot \text{ yr}^{-1}$, the western galaxy appears to have had its global star formation enhanced by the merger activity. Though lacking a major nuclear starburst, the western galaxy may be experiencing slight disk perturbations that lead to cloud-cloud collisions throughout the disk, resulting in the observed widespread distribution of star formation in this galaxy.

The organization and symmetry exhibited by the galaxies in IRAS 10190+1322 suggests that this galaxy pair is closing in for a second encounter, having spent a few dynamical timescales apart following the initial encounter. This statement is based on the assumption that merging galaxies are ultraluminous only *after* the first close encounter, and that the symmetric, orderly appearance of these galaxies can only mean that the galaxies have had enough time to regroup after their first encounter. The simulations by Mihos & Hernquist (1996)—especially the prograde/retrograde encounters as seen just prior to the second encounter—very much resemble the IRAS 10190+1322 system. This scenario raises a few important issues. First, how does one tell whether a double-galaxy merger is being seen early or late in the merger process? Besides the organized velocity fields and symmetric inner isophotes, what large scale morphological signatures might there be to indicate the age of a merger? Does IRAS 10190+1322 display such features? The second major issue is: why now? Why wait until just *before* the final merger to become ultraluminous?

A simple statement regarding the young versus old mergers is that tidal deformations in young mergers ought to be small and of high surface brightness. By the time the galaxies are approaching the final merger, tidal debris is expected to be strewn over relatively large scales, and thus lower in surface brightness. IRAS 10190+1322 does not, in fact, appear to have any significant tidal structure, though deep visual imaging is not available for this system. Inspection of the digitized Second Palomar Sky

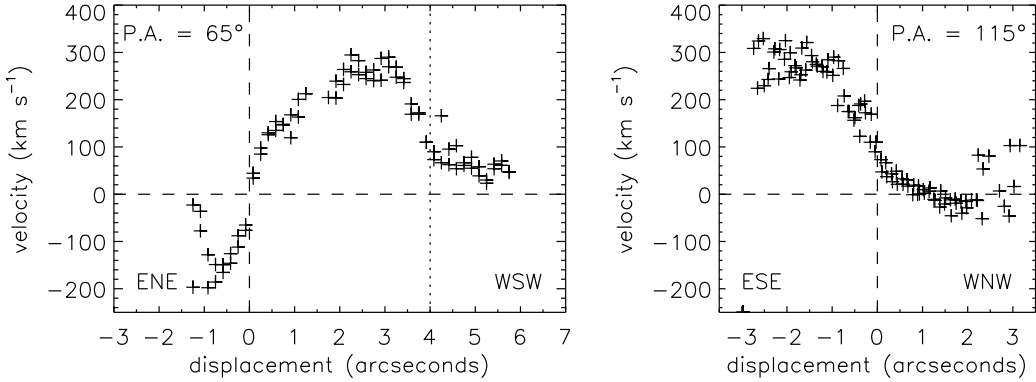


FIG. 9.—Position-velocity plots of IRAS 10190+1322, with the left-hand figure representing a cut through both nuclei simultaneously, at the field's long-axis position angle of 65° . The curve on the right is along a position angle rotated 50° relative to the first, showing the full velocity extent of the western galaxy. Both plots share the same vertical scale, and the zero point is placed at the velocity of the eastern continuum peak. The dotted line in the left-hand plot indicates the spatial position of the western nucleus.

Survey red plates does show some hint of tidal arcs around the western galaxy, but at a level only slightly above the noise. A moderately deep J band image taken in poor seeing conditions also shows a few tenuous wisps of light near the western nucleus, namely at radii of $9''$ and $17''$ from the western galaxy, at position angles of 205° and 315° , respectively.

The question regarding why IRAS 10190+1322 has waited until this late time in the merger sequence to initiate ultraluminous activity is difficult to answer. For reasons discussed at length in Section 4, the ultraluminous phase must be short relative to the merger timescale, assuming that star formation is responsible for the power generation. Because the disks have yet to experience their second disruptive passage, it is assumed that the observed ultraluminous phenomenon is in response to the earlier encounter, perhaps as long as $5\text{--}10 \times 10^8$ yr ago. Encounter geometry may play a significant role in determining the time of the onset of ultraluminous activity, though many other factors specific to the constituent galaxies including galaxy structure, initial gas distribution, etc. may also be very important. If the eastern galaxy is not purely prograde, then the weaker tidal perturbation may require more time to permit the development of significant accumulations of gas in the nuclear regions.

3.3. IRAS 20046–0623

3.3.1. Morphology of Continuum & Line Emission

The morphologically peculiar IRAS 20046–0623, classified as a starburst from unpublished visual spectra (Strauss 1993), is displayed in Figure 10. The galaxy has a continuum shape at first appearing like a warped disk, with one prominent tidal tail extending to the north at the eastern end of the continuum bar. The $\text{H}\alpha$ image is seen to share a somewhat similar appearance to the r band continuum, though the peak line emission is located on the eastern end of the continuum bar. The tidal tail shows emission in $\text{H}\alpha$, though displaced about $0''.6$ to the west of the continuum ridge.

The integral field data for IRAS 20046–0623 are presented in Figure 11. Here, the $\text{Pa}\alpha$ emission and continuum emission are largely exclusive of each other, in that the peak of the $\text{Pa}\alpha$ emission coincides with the outer edge

of the continuum bar, and the peak of the continuum emission is located at the edge of the strong $\text{Pa}\alpha$ structure. Faintly visible is a patch of $\text{Pa}\alpha$ emission to the northeast, coinciding with the $\text{H}\alpha$ emission in the tidal tail.

3.3.2. Extinction & Star Formation

The total $\text{Pa}\alpha$ flux in a $5'' \times 2''.5$ box, oriented east-west and capturing the majority of the $\text{Pa}\alpha$ emission, measures $3.5 \times 10^{-17} \text{ W m}^{-2}$. Comparing this to the $\text{H}\alpha + [\text{N II}]$ flux in a similar aperture yields a comparable flux of $3.6 \times 10^{-17} \text{ W m}^{-2}$. This implies a lower limit on the average extinction to the line emitting gas of $A_V > 3.5$ mag, using the same assumptions detailed in Section 3.1.2. A $1''.5 \times 1''.5$ aperture centered on the peak emission yields $\text{Pa}\alpha$ and $\text{H}\alpha + [\text{N II}]$ fluxes of $1.75 \times 10^{-17} \text{ W m}^{-2}$ and $7.9 \times 10^{-18} \text{ W m}^{-2}$, respectively, implying an extinction of $A_V > 4.6$ mag to this line emission.

The global star formation rate calculated from the $\text{Pa}\alpha$ flux, following the method presented in Section 3.1.2, is about $40 M_\odot \text{ yr}^{-1}$ for IRAS 20046–0623, uncorrected for extinction. Using the average visual extinction of 3.5 mag, and taking $A_{\text{Pa}\alpha} = 0.145 A_V$ (interpolated from the extinction law in Rieke & Lebofsky 1985), this value becomes $\sim 65 M_\odot \text{ yr}^{-1}$, which approaches the expected SFR for ultraluminous galaxies.

The tidal tail extending to the north also shows appreciable line emission, as seen by the $\text{H}\alpha + [\text{N II}]$ light in Figure 10. Computing a SFR directly from this light yields $1.4 M_\odot \text{ yr}^{-1}$, uncorrected for reddening. Assuming a moderate extinction of $A_V = 1$ mag boosts this to a few $M_\odot \text{ yr}^{-1}$. While not as high as the SFR in the tail of IRAS 01521+5224, this is still higher than previously observed in tidal tails (Hibbard & van Gorkom 1996; Mihos & Bothun 1998). As with IRAS 01521+5224, this high rate of star formation could be associated with the crossing orbits in very young tails (cf. Toomre & Toomre 1972; Wallin 1990)—consistent with the estimated very early age of this merger, as discussed below.

3.3.3. Merger Geometry & Age

IRAS 20046–0623 presents a complex velocity field, as seen in Figure 11. There are two primary axes of importance, which align with the major and minor axes of the continuum morphology. On the western side of the galaxy

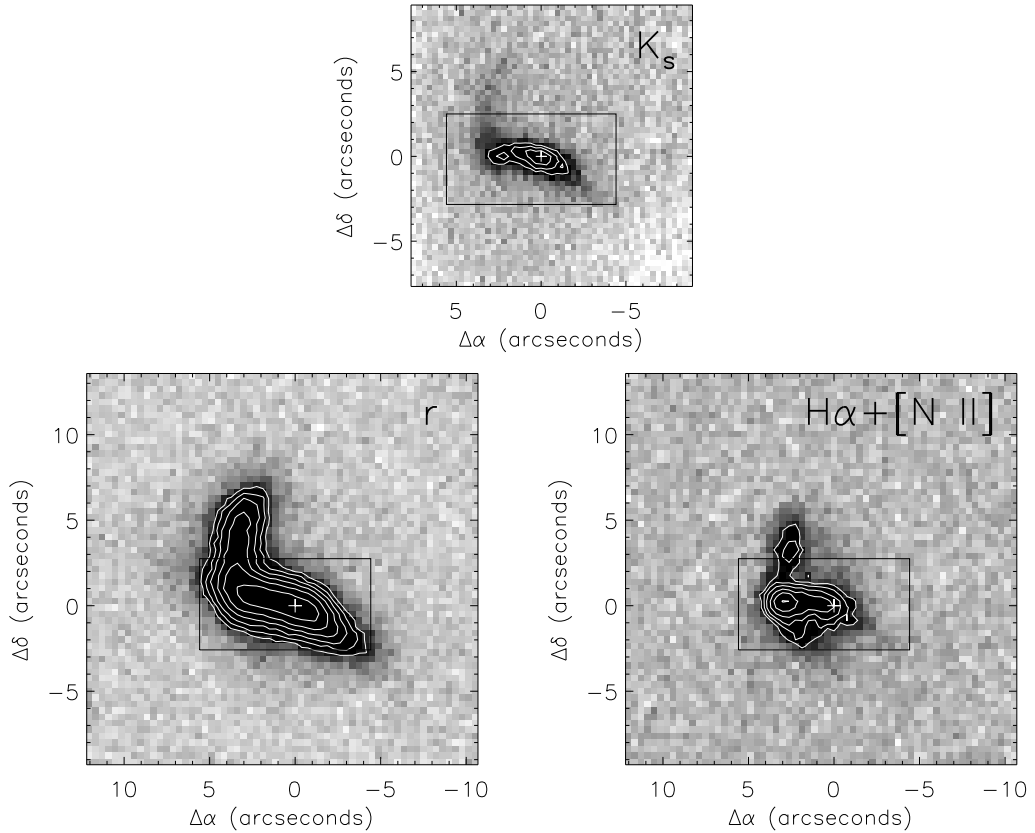


FIG. 10.— Continuum and $\text{H}\alpha + [\text{N II}]$ images of IRAS 20046–0623. The tidal tail extending to the north is much more prominent in the r band image than in the K_s image, suggesting that it is comprised of young stars. The $\text{H}\alpha$ emission peaks at the eastern end of the continuum bar, and line emission is also seen following the tidal tail. The cross indicates the position of the near-infrared peak, and the rectangular box represents the PIFS field. North is up, and east is to the left.

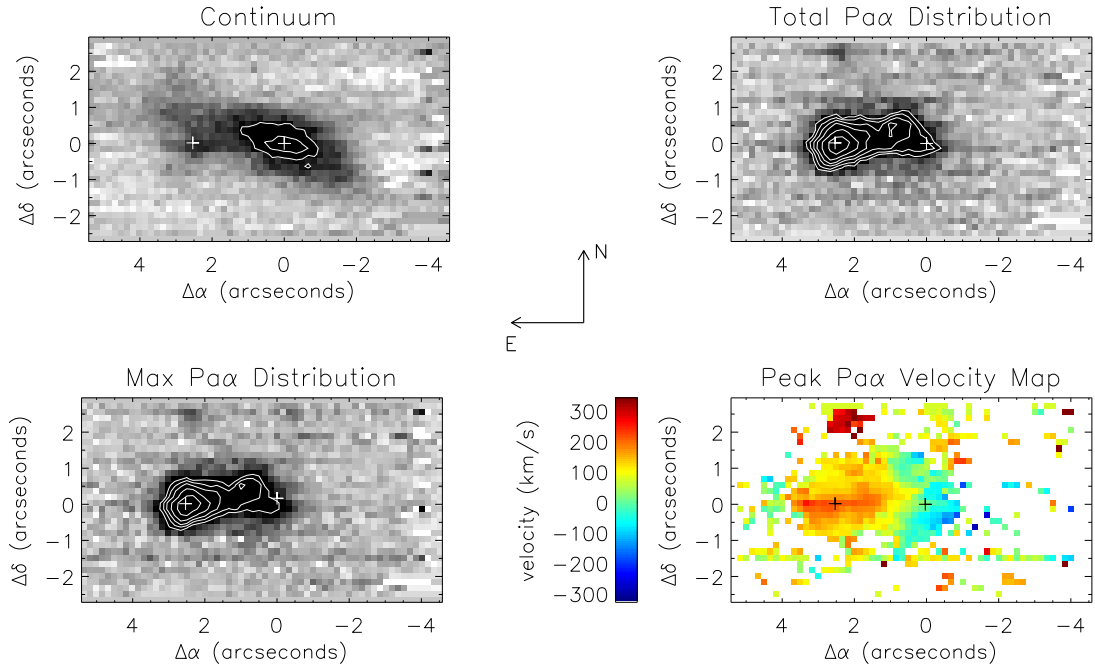


FIG. 11.— Integral field data for IRAS 20046–0623. Description of the four images follows from the Figure 2 caption. Crosses indicate the positions of the continuum and $\text{Pa}\alpha$ peaks. North is up, and east is to the left.

there exists a velocity gradient with iso-velocity contours running roughly parallel to the minor axis. This part of the velocity field looks like rotation of the disk. The east-

ern side, where the $\text{Pa}\alpha$ is the strongest, has an orthogonal axis of symmetry—along the major axis. Moreover, the velocity field in this region is centrally peaked rather

than linear in nature, with a maximum velocity along the central axis and lower velocities to either side.

The nature of the velocity fields may be seen more clearly in Figure 12, which presents position-velocity plots in the east-west and north-south directions, centered on the continuum peak and $\text{Pa}\alpha$ peak, respectively. Along the major axis, the velocity profile has a very linear segment spanning 250 km s^{-1} , followed by a very flat distribution across the $\text{Pa}\alpha$ peak. The trailing off to the blue at the very eastern end of the position-velocity diagram is not associated with strong $\text{Pa}\alpha$ emission, and is possibly contaminated by the presence of an OH airglow line at the wavelength corresponding to $\sim 50 \text{ km s}^{-1}$. Ignoring the blue down-turn to the east, the velocity profile of the east-west position-velocity plot as the appearance of a flattened rotation curve, which is truncated on the western end. In the north-south position-velocity plot, the central hump in the velocity field is clearly seen.

The distribution of velocities in IRAS 20046–0623 is not characteristic of any simple mode of motion. However, as with IRAS 01521+5224, the placement and velocity of the tidal tail feature in IRAS 20046–0623 can provide some clue to the age and geometry of this merging system. First, the relative shortness and high surface brightness of the tail, together with the distorted appearance of the continuum bar, argue that this system is relatively young, being viewed soon after the first encounter. The projected length of the tail, roughly 7 kpc, is traveled in $3\text{--}5 \times 10^7 \text{ yr}$ at typical tail speeds of $150\text{--}250 \text{ km s}^{-1}$. The near-straightness of the tail, plus its high recessional velocity—seen as a cluster of points to the north in Figure 12—argues that the parent galaxy is seen nearly edge-on, from a vantage point close to its rotational plane. The tail, in fact, should then point at the location of the parent galaxy’s nucleus. While there is no prominent continuum peak along the tail centerline, the $\text{Pa}\alpha$ peak does in fact lie very close to this line.

The rotational axis associated with the western continuum peak is orthogonal to both the kinematic axis of symmetry to the east and the rotational plane of the eastern galaxy, inferred from the tidal tail. There are then almost certainly two distinct galaxies overlapping to form the observed configuration. The absence of a prominent continuum peak to the east is at first disconcerting, but the $\text{Pa}\alpha$ peak belies its presence. With $\gtrsim 5$ mag of visual extinction to the line emission, and therefore almost a magnitude of extinction at $2 \mu\text{m}$, the absence of an obvious continuum peak is less startling. The western galaxy, which by its elongation appears to be seen nearly edge-on, could provide a screen of dust—obscuring the continuum peak and diminishing the dominant $\text{Pa}\alpha$ found in the eastern galaxy.

A picture can be developed that may account for the various observed features. Because of the extinction, we assume the western galaxy to be in the foreground. The western galaxy is almost edge on, so that we are looking nearly along its rotational plane. The eastern galaxy, mostly hidden behind the disk of the western galaxy, is also seen more-or-less from within its rotational plane, owing to the straightness and recessional velocity of the tidal tail. The eastern galaxy, having a prominent tail developed rather rapidly following the first encounter, is

most likely highly prograde. If this is true, then as with IRAS 01521+5224, the eastern galaxy’s rotation plane is roughly aligned with the orbital plane, and we are looking from nearly within the orbital plane. This puts the western galaxy in a highly inclined orbit, explaining both the lack of a prominent tail and its tardiness at triggering any significant $\text{Pa}\alpha$ emission in the nuclear region. Figure 13 shows a depiction of the geometry of the IRAS 20046–0623 system, with views both onto the orbital plane, and from our vantage point.

The velocity field can also be understood to some degree in this picture. As a result of its prograde geometry, and therefore its efficiency at setting up transport of gas to the nucleus, the eastern galaxy has highly concentrated $\text{Pa}\alpha$ emission associated with its nucleus, the shape of which is seen to some extent through the foreground screen. The rotational signature of this nucleus ought to be red to the north and blue to the south, judging by the redshifted tail to the north. Notice in the velocity field of Figure 11 that exactly such a gradient is seen on the southern half of the eastern $\text{Pa}\alpha$ emission. The orientation of the western disk, with a major axis position angle of $\sim 75^\circ$, is placed such that the maximum extinction would be expected just to the north of the $\text{Pa}\alpha$ peak position. At this position, the diffuse emission in the western disk may dominate the $\text{Pa}\alpha$ flux, masking the rotation signature of the diminutive background line emission. With this in mind, the position-velocity plot on the right in Figure 12 can be understood as a superposition of two components. South of the spatial plot origin, the rotation curve of the background nucleus is seen, but then quickly damped out to the north, where the emission from the diffuse western disk dominates, and the associated extinction suppresses the background flux from the eastern galaxy.

With a better understanding of the velocity field in IRAS 20046–0623, a more representative position-velocity plot can be generated for the individual galaxies. In Figure 14 we assume a 75° position angle for the western galaxy, and also plot a likely extension of the rotation curve for the eastern galaxy. Besides lying along the major axis of the K_s band continuum emission, the 75° position angle is in good agreement with some of the subtle features of the velocity field in Figure 11. In particular, one sees a demarcation between blue and yellow to the southeast of the western nucleus that is indeed perpendicular to this position angle. Also, the bluest emission lies to the southwest of the nucleus, rather than directly west. The blue-colored region in the velocity field to the north of the western nucleus does not immediately fit into the scheme, and its nature is unknown.

Under the present geometrical interpretation, IRAS 20046–0623 is a very young interaction, being seen only a few $\times 10^7 \text{ yr}$ after passing through pericenter, during the first encounter. Not only does the tidal tail morphology, velocity, and length support this idea, but the following very simple argument strengthens this interpretation. The eastern galaxy is highly obscured, presumably by the disk of the western galaxy—placing the eastern galaxy in the background. The relative velocities of the eastern and western galaxies are such that the eastern (background) galaxy is receding, as can be seen in Figure 14. Therefore, the two galaxies are growing further apart, as would

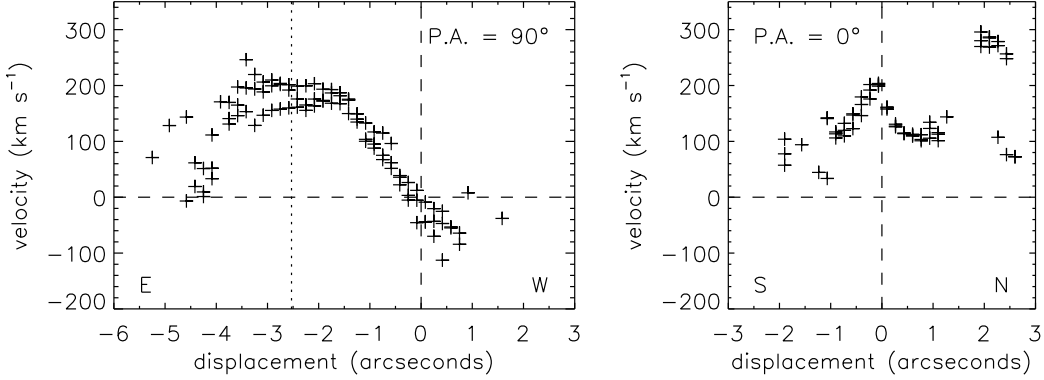


FIG. 12.— Position-velocity plots through two different axes of IRAS 20046–0623. The plot on the left represents a $0''.5$ slit at a position angle of 90° through the continuum peak. The right-hand plot is along the orthogonal direction through the Paa peak. Notice the central hump at the position of the Paa peak, and the tidal tail emission redshifted by $\sim 300 \text{ km s}^{-1}$ relative to the continuum peak’s central velocity. The dotted line in the left-hand plot indicates the spatial position of the Paa peak.

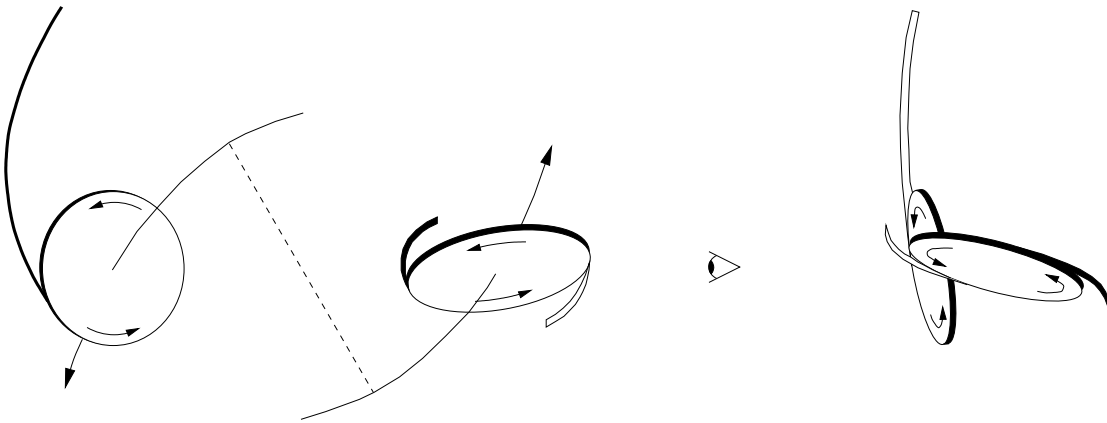


FIG. 13.— The proposed geometry for the IRAS 20046–0623 merger, which is able to reproduce the observed morphology and kinematics. At left is a view more-or-less onto the orbital plane, and at right is the view we have of the system, which is from a vantage point to the right of the left-hand figure, near the plane of the paper. The orbital tracks and time since pericentric passage are only suggestive here. Note that the galaxy corresponding to the one with the bright tail and nuclear starburst is almost purely prograde in this geometry.

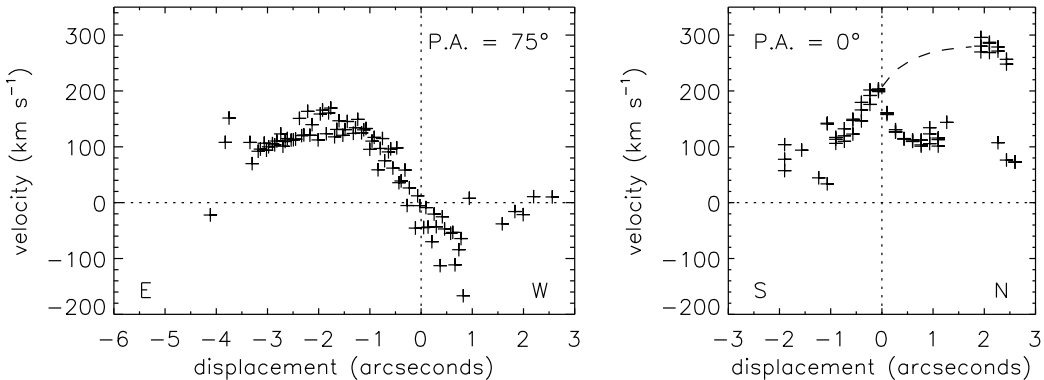


FIG. 14.— Position-velocity plots for IRAS 20046–0623, again along two axes, but this time considering the model that has been developed for the merger geometry. The left-hand plot now shows the rotation curve for the western galaxy, along a position angle of 75° . The right-hand plot shows the likely extension of the rotation curve for the eastern galaxy, which is masked by the dominant emission (plus extinction) from the western disk.

be expected if these galaxies are seen just after a close encounter.

3.4. IRAS 17574+0629

3.4.1. Morphology of Continuum & Line Emission

IRAS 17574+0629 is a morphologically disturbed galaxy classified as an H II galaxy by the visual spectra of Kim, Veilleux, & Sanders (1998). The continuum images of IRAS 17574+0629 in Figure 15 show a single distorted nucleus with what appear to be two tidal tail features extending to the north and to the east. The $\text{H}\alpha + [\text{N II}]$ im-

age shows a prominent emission peak slightly offset from the continuum peak, plus a large region of diffuse emission to the northeast. Figure 16 shows the continuum as constructed from the PIFS datacube, along with the appearance of $\text{Pa}\alpha$ in the system. Similar to the $\text{H}\alpha$ image, a large gaseous nebula is seen in $\text{Pa}\alpha$ to the northeast, roughly in the direction of the tidal features. The detailed distribution of the $\text{Pa}\alpha$ nebula does not, however, exactly trace the positions of the diverging tidal features, but rather appears to be shaped like an edge-brightened bubble.

3.4.2. Extinction & Star Formation

The $\text{Pa}\alpha$ distribution can be broken into two regions: the nuclear region, and the extended emission to the northeast. The $\text{Pa}\alpha$ flux in a $3'' \times 3''$ box aperture around the nuclear emission is $4.2 \times 10^{-17} \text{ W m}^{-2}$, while the entire field has $\sim 25\%$ more total flux. Similar apertures on the $\text{H}\alpha + [\text{N II}]$ emission measure 6.7×10^{-17} and $1.3 \times 10^{-16} \text{ W m}^{-2}$, in the same order. A lower limit to the average extinction, using the large aperture measurement, is $A_V > 2.1$ mag, while the nuclear emission gives $A_V > 2.8$ mag. Given the flux ratios, this implies an extinction to the diffuse emission region of $A_V > 0.8$ mag. A ratio of the $\text{Pa}\alpha$ and $\text{H}\alpha + [\text{N II}]$ line images shows the extinction to be separately uniform across both the diffuse region and across the nuclear region, with typical deviations on the order of 0.2 mag.

The total $\text{Pa}\alpha$ emission, when converted to a global star formation rate in the manner outlined in Section 3.1.2, yields $103 M_\odot \text{ yr}^{-1}$, making this the most prodigious star forming galaxy in the sample, assuming that star formation is indeed responsible for the $\text{Pa}\alpha$ emission. This galaxy is also slightly more infrared-luminous than the other three galaxies in the sample. Applying the measured extinction to the $\text{Pa}\alpha$ flux results in a total SFR of $\sim 150 M_\odot \text{ yr}^{-1}$, with $\sim 85\%$ of this coming from the $3'' \times 3''$ aperture around the nuclear region.

3.4.3. Merger Geometry

Of this sample, IRAS 17574+0629 is the most difficult to understand in terms of its status as a galactic merger. As mentioned in Section 3.4.1, the morphology of the line emission is suggestive of an intense nuclear source accompanied by a large bubble of expanding gas. The kinematic portrayal of the line emission in Figure 16 appears quite complex, and does not lend immediate support this picture. An expanding bubble may be expected to display a uniform velocity gradient along the axis of expansion, which would be to the northeast in this case. The velocity field does not show such an orderly trend. The nuclear emission seems to exhibit a rotation signature in the north-south direction, but the velocity field of the diffuse emission is rather twisted and difficult to interpret.

An interesting feature of the IRAS 17574+0629 velocity field is the multi-valued nature to the immediate southeast of the nucleus. This can be seen more clearly in the two-dimensional spectra of Figure 17, especially in the three lower left panels. The red nuclear component clearly dominates the emission, and is the component represented in the velocity map of Figure 16, concealing the velocity structure of the weaker blue component.

In attempting to construct a conceptual model accounting for the gas motions, one must take the appearance of the two-dimensional spectra into consideration, as the blue component underlying the brighter red component seen in Figure 17 appears to be physically associated with the redder emission to the northeast, owing to the fact that a single, continuous gas component smoothly connects these two regions. Note the consistent appearance of the red-to-blue velocity gradient seen in the faint emission of Figure 17 in all of the synthesized slits.

In order to isolate this gaseous component of the system, the dominant $\text{Pa}\alpha$ peak was subtracted from the datacube by fitting and subtracting Gaussian profiles with elliptical cross sections in the individual two-dimensional spectra. This procedure was carried out in the two-dimensional plane represented by Figure 17, the result of which is also displayed here. The structure of the $\text{Pa}\alpha$ nebula with the dominant peak removed appears in Figure 18. Judging by the appearance of the modified two-dimensional spectra in the datacube (Figure 17), we suggest that the image in Figure 18 roughly corresponds to the true morphological character of a physically connected structure in the galaxy.

Figure 18 also presents the kinematic structure of the large $\text{Pa}\alpha$ nebula in the absence of the much brighter nuclear source. Now the velocity field appears more organized, with a distinctive V-shaped pattern aligned with—and roughly centered on—the nebula's major axis. Such a pattern could be consistent with the bubble description of the nebula, with a smooth gradient along the expansion axis. A trend from blue to red is seen to be present throughout the nebula as one moves away from the galaxy nucleus along the nebula's major axis. If this feature is indeed associated with an expanding bubble, then the observed geometry suggests that material is being ejected somewhat towards the observer, and slowing down as it gets farther from its source.

The bubble/outflow picture does not fully satisfy other features of the appearance of IRAS 17574+0629. In particular, the r band morphology in Figure 15 is fairly similar to that of IRAS 20046–0623 (Figure 10, Section 3.3). Namely, there is a short stub of a tidal tail extending to the north, and even the little curl of continuum emission at the southeastern tip finds a similar analog in IRAS 20046–0623—which appears to be a very young merger experiencing its first encounter. Indeed, the lack of low surface brightness emission around the perimeter, much like in IRAS 01521+5224, argues that this too is a first encounter ULIRG. Yet there is no obvious second galaxy. It is possible that we are the victim of projection, wherein the second galaxy lies just behind the visible galaxy. In fact, one clue that may support this claim is the offset of the $\text{Pa}\alpha$ line emission peak from the continuum center by about one arcsecond to the south, corresponding to more than 1.5 kpc. It is hard to imagine the circumstances that might produce an offset this large in a $150 M_\odot \text{ yr}^{-1}$ starburst. We would expect energy production on this scale to be associated with a mass center capable of gathering the fuel supply.

Another clue in this vein may come from the $\text{Pa}\alpha$ image with the dominant nuclear emission removed (Figure 18). Here, the peak of the $\text{Pa}\alpha$ emission lies $0''.5$ to the northeast of the continuum peak, or approximately 1 kpc away.

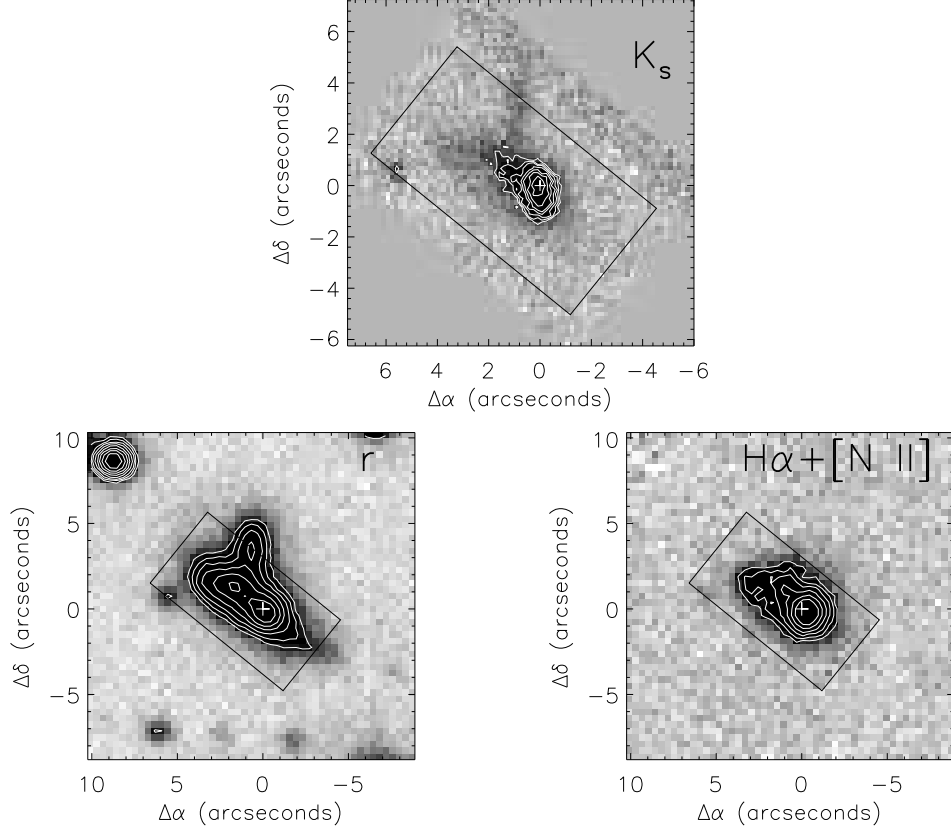


FIG. 15.— Continuum and $\text{H}\alpha + [\text{N II}]$ images of IRAS 17574+0629. Two tenuous tails are seen extending to the east and north. The $\text{H}\alpha$ morphology indicates the presence of a large, diffuse nebula to the northeast. The rectangular box indicates the position and orientation of the PIFS field. The cross marks the position of the near-infrared peak. North is up, and east is to the left.

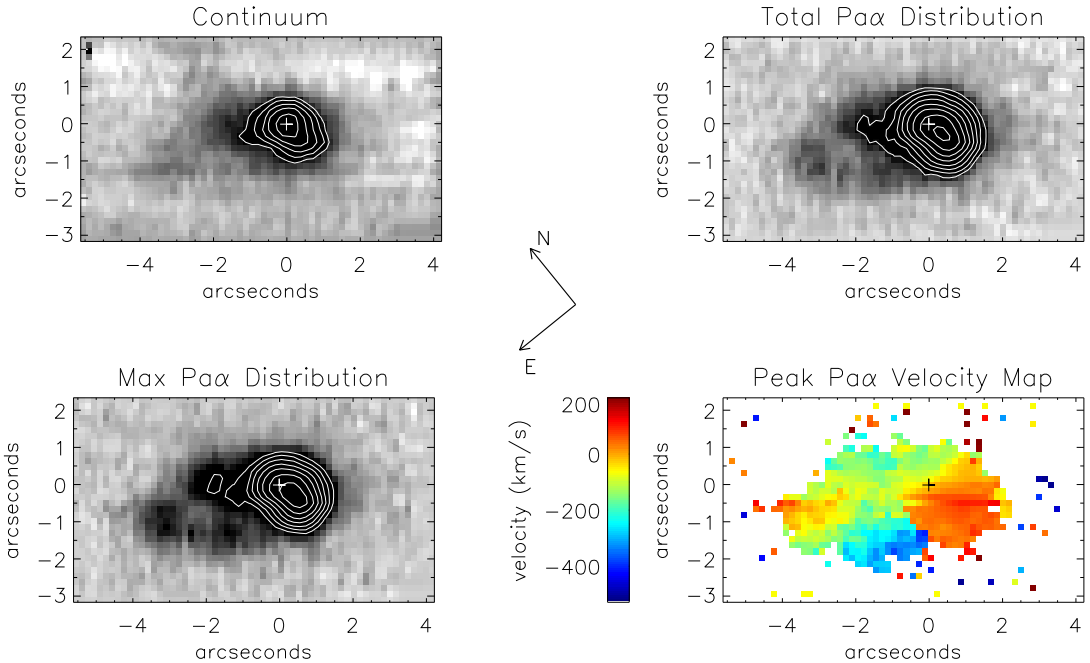


FIG. 16.— Integral field data for IRAS 17574+0629. Description of the four images follows from the Figure 2 caption. Field orientation is indicated by the arrows, with “left” corresponding to a position angle of 51° . The cross indicates the position of the continuum peak.

In total, the bright nuclear emission and the less prominent diffuse peak lie at least 2 kpc apart in the plane of the

sky. Could these two emission line features point to the locations of the parent galaxies? The continuum shape is

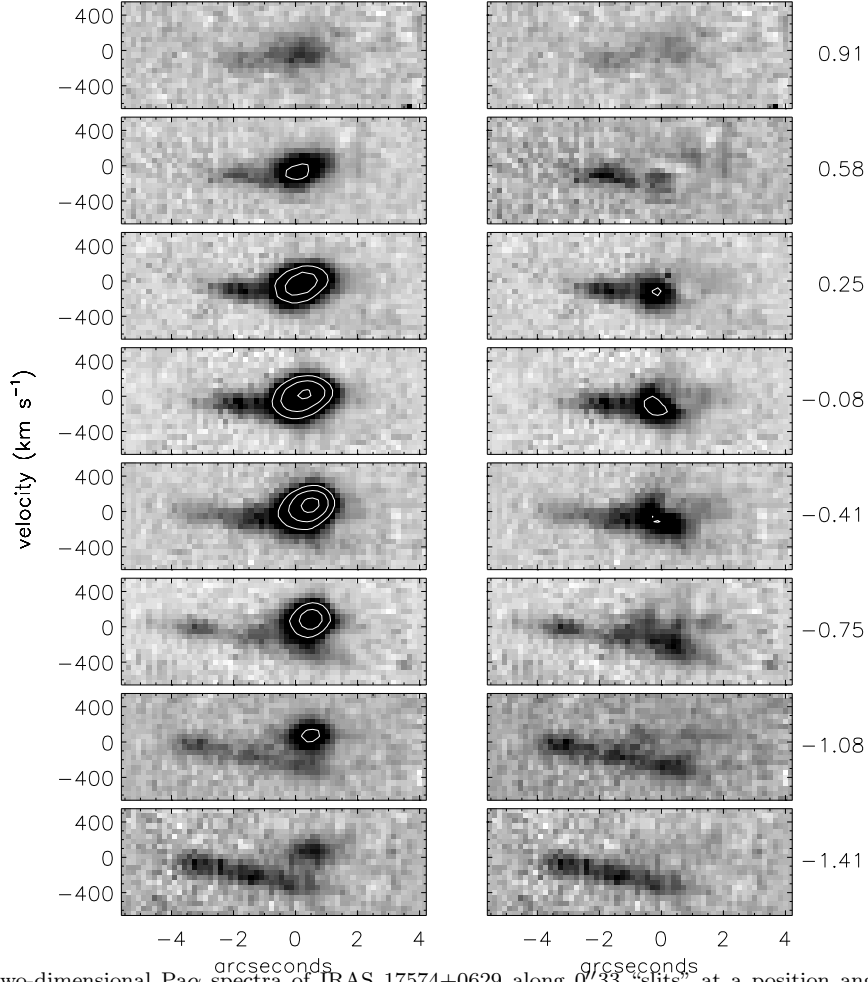


FIG. 17.— A series of two-dimensional $\text{Pa}\alpha$ spectra of IRAS 17574+0629 along $0''.33$ “slits” at a position angle of 51° . Each panel is spatially offset from the adjacent one by $0''.33$, with the top-to-bottom progression moving from northwest to southeast. The left-hand column depicts the continuum-subtracted total line emission, while the right-hand column displays the same emission with the dominant nuclear $\text{Pa}\alpha$ component subtracted. Note the multi-velocity nature of the $\text{Pa}\alpha$ emission in the left-hand column at the position of the nucleus. The blue component is seen to be physically connected to the red component that appears on the left side of the images in Figure 16. Each panel spans 10 arcseconds horizontally and 1250 km s^{-1} vertically. Contours are placed at multiplicative factors of two apart. The spatial coordinates indicated at bottom and right are referenced to the coordinates used in Figure 16.

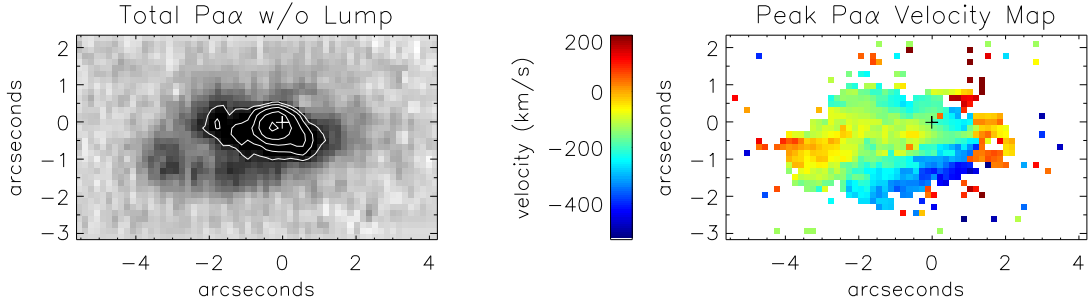


FIG. 18.— Morphology and velocity field of IRAS 17574+0629 after subtracting a mathematical representation of the dominant nuclear $\text{Pa}\alpha$ component from the two-dimensional spectra comprising the datacube. The underlying velocity field shows an order that is not immediately apparent from Figure 16.

not entirely inconsistent with this idea. The K_s peak in Figure 15 has a north-south elongation which could correspond to the nuclear $\text{Pa}\alpha$ source—with its north-south velocity gradient—and a spur to the northeast roughly aligned with the strong $\text{Pa}\alpha$ feature as seen in the absence of the dominant nuclear component (Figure 18).

If indeed we see two superimposed galaxies, then the

tidal features can help distinguish possible configurations. The northern tail is almost certainly associated with the dominant $\text{Pa}\alpha$ peak, as it is roughly aligned with the rotation axis of this feature. Given the sense of rotation—redshifted to the south—the tail would be blueshifted and in front of the galaxy. In a young encounter, this would put the north-south galaxy in front of the more diffuse galaxy

with the northeast-southwest orientation. This arrangement goes against the simple extinction difference between the two, though a high nuclear extinction to the concentrated emission is by itself rather typical in ULIRGs. However, the two-dimensional spectra in Figure 17 shows that the extinction to the diffuse component does not appear to be affected by the superposition of the bright nuclear emission. This can be seen in the three lower left panels, which shows no apparent decline in the strength of the diffuse emission at points that are spatially coincident with the bright component.

Determining an age for the IRAS 17574+0629 encounter is impossible without a clear understanding of its current merger state. Conflicting clues lead to both early and late assessments. The short tails, lack of diffuse emission surrounding the ensemble, possible double nucleus belied by the $\text{Pa}\alpha$ peaks, and very close resemblance to the IRAS 20046–0623 system would argue for a young merger. The lack of two nuclei, the incompatibility of extinction trends with attempts to reconstruct the merger state based on kinematics, and the lack of bright line emission in the northern tidal tail (like that seen in IRAS 20046–0623 and IRAS 01521+5224) argue that this is a late stage, post-merger system.

4. DISCUSSION

Ultraluminous infrared galaxies are rare, occupying the extreme tail of the infrared galaxy luminosity function (Soifer et al. 1987; Sanders & Mirabel 1996). Special circumstances are required to boost the luminosity in these systems by as much as two orders of magnitude over their normal levels. Clearly the merging process is the key, as the overwhelming majority of ULIRGs show evidence for recent or ongoing merger activity. An important question is: where, and in what form is the energy produced that is being radiated at far-infrared wavelengths as thermal dust emission? The answer to this question is obscured by the very dust that is radiating the far-infrared flux.

4.1. Physical Size & Rate of Star Formation in ULIRGs

In each of the ULIRGs observed in this sample, $\text{Pa}\alpha$ emission is seen spread over many kiloparsecs, implying widely distributed star formation. But each one of these systems also exhibits a compact source of $\text{Pa}\alpha$ emission with a flux comparable to—and usually exceeding—the integrated flux of the extended line emission. The ubiquitous appearance of a bright nuclear $\text{Pa}\alpha$ feature which dominates the total star formation is an important result. Even these spatially complex ULIRGs, selected for their extended $\text{Pa}\alpha$ emission, are currently powered by concentrated nuclear starbursts. This echoes a similar finding among a much larger sample of ULIRGs as reported by Murphy et al. (2001). Observations of ULIRGs at mid-infrared wavelengths by Soifer et al. (2000) and at submillimeter wavelengths by Sakamoto et al. (1999) also support this finding, with typical mid-infrared core sizes of < 200 pc. Also important is the fact that there typically exists at least one magnitude of extinction at $2 \mu\text{m}$ to the nuclear line emission regions, if the total SFR is to account for the high luminosity. Similar results have been obtained via longslit spectroscopy of ULIRG samples (Goldader et al. 1995, Murphy et al.). This is especially relevant when

searching for spectral signatures of active galactic nuclei (AGN) within ULIRGs.

If the far-infrared luminosity in ULIRGs is completely a product of star formation, then it is possible to calculate the rate of star formation required to produce the observed power output. Several such estimates have been made, establishing an order-of-magnitude expectation for ULIRG star formation rates. The first and simplest estimate, from Scoville & Young (1983), computes the rate of mass consumption from O, B, and A stars via the CNO cycle, yielding an expected $77 M_\odot \text{ yr}^{-1}$ for a total luminosity of $10^{12} L_\odot$. This approximation is very nice in its simplicity, though probably an underestimate because some of the mass consumption goes into making lower mass stars that do not contribute significantly to the total luminosity. Hunter et al. (1986) integrate the stellar luminosity with an assumed initial mass function (IMF) to obtain $L_{\text{ir}} = 10^{12} L_\odot$ with $260 M_\odot \text{ yr}^{-1}$, assuming all the luminosity is processed by dust and emitted in the far-infrared. Inoue, Hirashita, & Kamaya (2000) perform a similar, more flexible analysis, arriving at $330 M_\odot \text{ yr}^{-1}$, though a rate as low as $200 M_\odot \text{ yr}^{-1}$ can be obtained by pushing the model to extremes. For our purposes, it is sufficient to say that ULIRGs require an integrated star formation rate of $\sim 200 M_\odot \text{ yr}^{-1}$.

As pointed out above, each of the ULIRGs in this sample exhibit both widespread and concentrated nuclear star formation, as traced by $\text{Pa}\alpha$ emission. Comparison of $\text{Pa}\alpha$ fluxes to $\text{H}\alpha$ fluxes (or 6 cm radio continuum in the case of IRAS 10190+1322) reveals more extinction towards the sites of concentrated emission ($A_V \approx 3 - 7$ mag) than to the diffuse nebular regions ($A_V \lesssim 1$ mag). This is to be expected if the nuclear emission arises from a very large, dense cloud of accumulated gas and dust. The star formation rates in the extended nebular regions tend to be $10 - 20 M_\odot \text{ yr}^{-1}$ —far short of the energy budget required to produce ultraluminous emission. These SFR numbers could be modified upward slightly by extinction corrections, though not by the factor of ten necessary to result in ultraluminous far-infrared flux. On the other hand, the nuclear $\text{Pa}\alpha$ emission translates to typical SFR values of $50 - 80 M_\odot \text{ yr}^{-1}$, after applying extinction corrections measured from the $\text{H}\alpha/\text{Pa}\alpha$ ratio. Though this is still a factor of 3–4 short of the ULIRG SFR requirement, it is clear that the bulk of the power comes from the nuclear emission regions. The remaining deficit can then be attributed to high levels of extinction in the interior of the nuclear gas concentration, such that only the outer regions of line emission are seen—even at the wavelength of $\text{Pa}\alpha$, as previously suggested by Goldader et al. (1995).

4.2. Ages of ULIRGs

The present observations have resulted in understanding the merger geometries of the constituent galaxies in a few ULIRGs. Knowing how the galaxies are oriented and how they are moving relative to one another allows one to roughly identify the time within the merger history at which we view these systems. Measured lengths of tidal tails together with recessional velocities yield estimates for the age of formation of these structures. Comparisons to the gas morphologies in sophisticated merger models lend further support to the age estimates.

The selection of the sample ULIRGs based on their spatial and spectral complexity biases our sample in several fundamental ways. First, the morphology biases the sample galaxies to early merger states in which the constituent galaxies have been disrupted, yet have not coalesced into a post-merger remnant. Also, the selection of galaxies with complex morphologies, and whose two-dimensional spectra show large spatial extent and non-trivial velocity structures yields a sample that presents the greatest challenge to understand. Despite the latter effect, integral field spectroscopy has allowed some insight into the nature of these highly disturbed systems. One additional consequence of the selection based partly on morphological non-triviality seems to be a greater likelihood of chance superpositions, and alignment of our viewpoint with the orbital plane. This appears to play a role in at least two of the four galaxies in the sample.

The inferred young ages of IRAS 01521+5224 and IRAS 20046–0623 of a few $\times 10^7$ yr, reckoned since closest approach, demand a very fast response to the merger on the part of the gas. In order for the ultraluminous activity to commence so quickly after the first encounter, substantial quantities of disk gas must be very rapidly transported into the central regions. Additional evidence for very young ULIRGs was found by Mihos & Bothun (1998) via Fabry Perot imaging of four ULIRGs, one of which (IRAS 14348–1447) is believed to be seen just after the first encounter. Merger models tend to show later onsets of starburst episodes—both in terms of absolute age and with respect to the corresponding morphological merger stage. The models by Mihos & Hernquist (1996)—when scaled to Milky Way sized galaxies—show peak star forming activity no sooner than 1.5×10^8 yr after the first encounter, corresponding to a time when the galaxies are far apart, less distorted, and approaching their apocenter. Similarly, high concentrations of gas do not occur in the models of Barnes & Hernquist (1996) until at least 10^8 yr after closest approach.

In addition to the two cases of very young mergers, IRAS 10190+1322 appears to be seen at an intermediate age. The fact that the constituent galaxies appear symmetric and undisturbed (i.e., lacking obvious tidal features) supports this claim. In order to be ultraluminous, it is assumed that galaxies must have undergone at least one close passage—thus stimulating the concentration of gas to fuel the starburst. When two galaxies in an ultraluminous pair appear close together, then they have either just passed their first encounter or are closing in for the final merger. Just after first approach, the galaxies appear highly distorted, as seen both in our data and in merger simulations (e.g., Barnes & Hernquist 1996; Mihos & Hernquist 1996). Thus the IRAS 10190+1322 pair, with its organized morphology, has probably had at least a dynamical timescale to regroup following the initial encounter, and is now rapidly approaching the final merger.

As with the young mergers, IRAS 10190+1322 exhibits a disparity between observations and current models with regard to the time at which merging galaxies produce energy on ultraluminous scales. The model from Mihos & Hernquist (1996) ascribes an increase in the SFR relative to the pre-merger SFR of only a factor of five at times leading up to the final merger event when the model mor-

phology appears strikingly similar to IRAS 10190+1322. These models in general predict a significant burst in star formation either following closest approach, or upon final coalescence of the progenitor galaxies, depending on the structure of the galaxy. IRAS 10190+1322 occupies a time in the merger sequence at which models predict a minimum amount of star formation activity. Yet the ultraluminous status of the galaxy pair, plus the high rates of star formation observed via $\text{Pa}\alpha$ indicates by example that the ultraluminous phenomenon can occur even at this stage in the merger sequence.

Careful study of the symmetry within ULIRG pairs in imaging surveys suggest that ultraluminous activity just prior to a second encounter is not entirely rare. Other ULIRGs are seen in states that appear more consistent with a time just prior to final merger than a time shortly after a close approach. Figure 19 shows the range of estimated ULIRG ages, performed rather subjectively based on morphological clues provided in imaging surveys by Murphy et al. (1996), Sanders et al. (1988), and Carico et al. (1990). The time axis is cast in relative units where $t = 0$ corresponds to the initial encounter, and $t = 1$ relates to the time of final merger, roughly corresponding to $\sim 10^9$ yr. For the morphological age classification, warped isophotes and short, bright tails signal early-stage mergers, while symmetric isophotes and large-scale tidal debris signal late-stage mergers. Several ULIRGs were not easily classified by this scheme, thus they appear as unshaded bins on both the early and late sides of the distribution. One source of ambiguity often comes from the lack of obvious large-scale tidal structure, as this may simply result from insufficient imaging depth. Age classifications of double nucleus ULIRGs from the 2 Jy sample of Murphy et al. appear in Table 5. Details on the age classification and temporal scaling based on nuclear separation are covered in Appendix A.

These results suggest that the ultraluminous phase has a bimodal distribution in time, with some ULIRGs found at very early times, and most seen in the latest stages of the merger process—many of which are seen after the progenitor galaxies have joined. A few ULIRGs are also seen at intermediate times. The bimodality is a natural consequence of the fact that merging galaxies on highly eccentric trajectories spend most of their time far apart, coupled with the observation that few ULIRGs are found in widely separated double systems. Geometry is likely to play a big role in determining when or if ultraluminous activity occurs along the sequence prior to the final merger. Both of the very early mergers seen in the present sample are believed to have the ultraluminous activity associated with highly prograde galaxies. Tilted disks, such as the northern galaxy in IRAS 01521+5224 and the western galaxy in IRAS 20046–0623, have some star formation activity, mainly away from the nucleus. Perhaps these galaxies are not sufficiently perturbed to organize a central gas concentration, owing to the slower and weaker response of the tilted disks to tidal disruptions. Judging by the time distribution in Figure 19, it appears unlikely that a galaxy will enter an ultraluminous phase during the long interval after the initial encounter, if not immediately following first encounter. Thus highly tilted or retrograde galaxies that require more time to concentrate their gas supplies

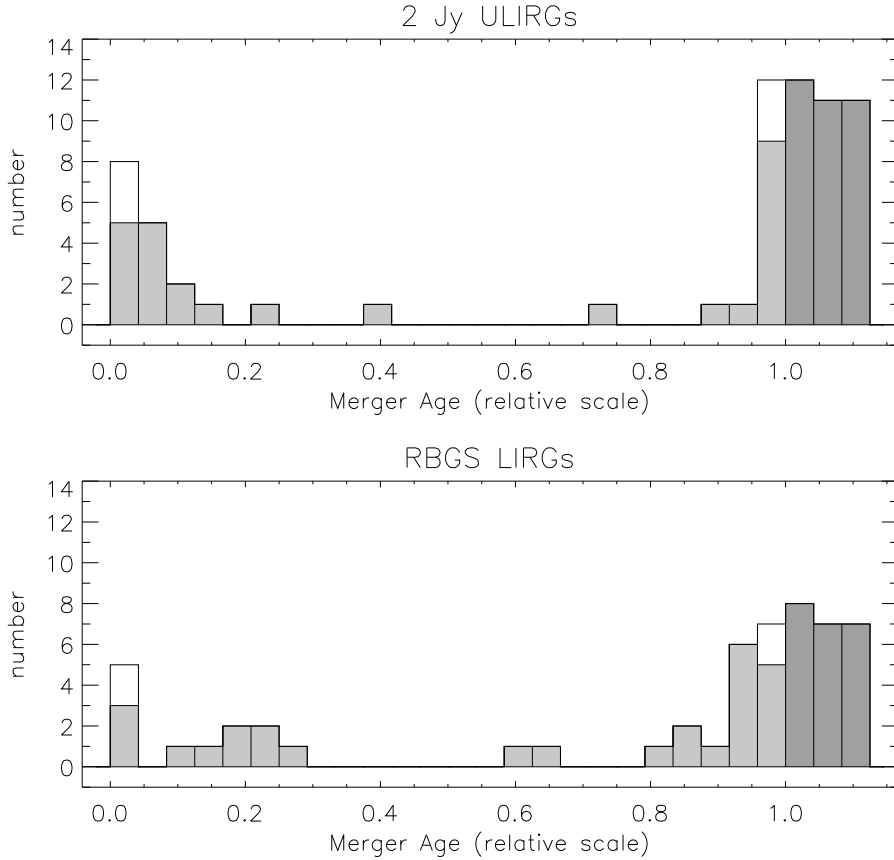


FIG. 19.— Histogram indicating how far ULIRGs are along the merging sequence, as estimated from morphologies in imaging studies. One unit of time corresponds to the encounter timescale, or roughly 10^9 yr. At the very least, ULIRGs appear to have a bimodal time distribution, though wide separation ULIRGs indicate the possibility that the ultraluminous phase may occur anywhere along the sequence. The final stage ULIRGs have been arbitrarily spread across three bins, for both scaling purposes, and also to reflect the timescale associated with this phase. These post-merger systems are indicated with darker colors. The unshaded boxes represent ambiguous cases that could not easily be classified as early or late interactions, and are accordingly placed at both early and late times. The same information is shown for a similar number of RBGS LIRGs, which exhibit a broader time distribution than ULIRGs. See Appendix A for details on age classification.

may fail to ever reach ultraluminous status prior to the final merger sequence.

Though the process of assigning early or late ages to ULIRGs based on morphology has been performed in a somewhat subjective manner, there appears to be a significant separation in the infrared luminosity distribution for the early population as compared with the rest of the sample. Figure 20 shows this split in histogram form. The late-encounter and post-merger systems are fairly uniformly spread across the luminosity range, while early-encounter ULIRGs are seen clustered near the low luminosity cutoff. Many previous studies of ULIRGs have associated nuclear separation with the time remaining until final merger, and have tried with little success to correlate properties such as infrared luminosity, molecular gas content, etc. with this timescale. However, grouping suspected early-encounter ULIRGs based solely upon morphology *does* tend to select lower luminosity systems than does a random sampling, indicating that the process of judging early or late encounters based on morphological signatures holds some merit. If the age classification scheme is approximately correct, then this luminosity separation indicates that early ultraluminous activity—usually found occurring on only one nucleus—is accompanied by less intense star formation activity than is typical in final merger events.

This could be because the early events do not concentrate the entire gas supply from both galaxies into the nuclear regions in a short period of time—as is likely the case during the final stages of a merger. The early-encounter ultraluminous galaxies may be experiencing rather short, intense bursts brought about by the rapid collection of *some* of the galaxy’s gas content into the nuclear regions in response to the sharp tidal perturbation caused by the recent close passage of the companion galaxy.

4.3. Ultraluminous Timescales & Evolutionary Scenarios

One possibility that deserves investigation is that the ULIRG phenomenon is episodic, with punctuated bursts of high intensity star formation, possibly occurring more than once along the merger sequence. The idea of repetitive starbursting was explored by Noguchi (1991), though in the context of cloud-cloud collisions, with most of the activity occurring in the late stages of the merger sequence. There exists a fundamental problem in the assumption that merging galaxies can remain ultraluminous throughout the entire merger process, from first encounter to final coalescence. Defined in this way, the merger process takes $5-15 \times 10^8$ years to complete, though an ultraluminous starburst, consuming a few hundred solar masses per year, depletes its molecular gas supply of a few $\times 10^{10} M_{\odot}$

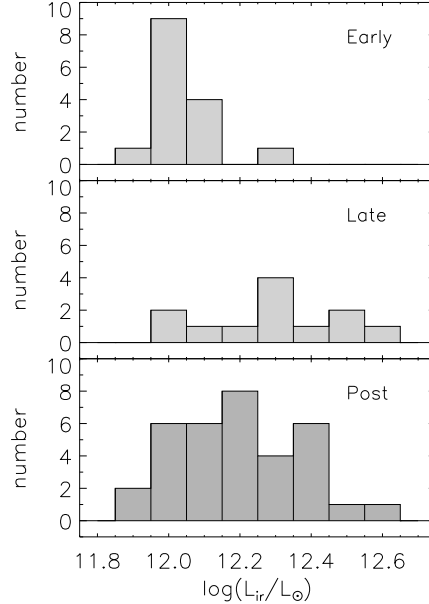


FIG. 20.— The distributions of infrared luminosity for the ULIRGs identified as early-encounter, late-encounter, or post-merger configurations.

in about 10^8 yr. Clearly then a starburst ULIRG cannot exist throughout the entire merger lifetime. The temporal distribution in Figure 19 strongly supports this conclusion, with a significant number of early ULIRGs, very few intermediate-age ULIRGs, and a preponderance of late-stage ULIRGs. The relative timescales of the starburst and merger processes suggest an ultraluminous duty cycle around 10–20%.

It is possible that individual mergers experience multiple ultraluminous bursts. Three natural time periods can be identified, corresponding to nuclear starbursts in each of the progenitor galaxies separately, plus a final event corresponding to the ultimate merger. Different orbital geometries, physical structures, and gas distributions can act to accelerate, prolong, or prevent the onset of ultraluminous activity in each of the parent galaxies, so that independent bursts do not necessarily happen simultaneously, if at all. As long as some appreciable fraction of the original gas mass is preserved in the disk of at least one of the galaxies, then it is highly likely that a final ultraluminous burst will occur around the time of the final merger. With the possibility of multiple ultraluminous bursts, the duty cycle for the ultraluminous phase may be anywhere from 10–30%.

It is entirely possible that the early bursts in ULIRGs are fueled only by gas from the inner disk. Gas in the outer disk may not have the chance to arrive at the nucleus before the waning tidal disruption is ameliorated by the inherent disk stability. Alternatively, energetic outflow phenomena, namely those produced by supernova winds, may sufficiently disrupt the transient nuclear fueling to terminate the early ultraluminous phase.

Early ultraluminous bursts, like the ones seen in the present data, are by no means ubiquitous among ULIRGs. Yet the fact that roughly half of the ULIRGs are seen in separated double nucleus systems, and that roughly one quarter are early-stage doubles according to Figure 19, indicates that a substantial fraction of the ULIRGs pass

through a pre-coalescence ultraluminous burst. The fraction of ULIRGs experiencing an early burst can not be ascertained directly from Figure 19 without knowledge of the relative lifetimes of the ultraluminous phases at early versus late times.

An important consideration to bear in mind is that ULIRGs do not have to originate from the collision between equally gas-rich galaxies. As long as one galaxy is gas-rich, and the two galaxies are comparable in overall mass, the tidal perturbations can act to fuel a nuclear starburst on the gas-rich galaxy only, or in the final merger if the first encounter is not sufficiently disruptive. This statement holds true if the primary mechanism for producing ultraluminous activity stems from dense nuclear accumulation of gas, and not from cloud-cloud collisions between the two galaxies. Note that each of the ULIRGs observed in the present sample appears to show true ultraluminous activity on only one galaxy nucleus, while the companion is often only moderately active. Similar asymmetric tendencies are observed among ULIRGs in the light of H α (Armus, Heckman, & Miley 1990), and—more importantly—in quantities of molecular gas (Trung et al. 2001).

4.4. Can LIRGs Be “Resting” ULIRGs?

LIRGs are defined as galaxies with $10^{11.3} L_{\odot} < L_{\text{ir}} < 10^{12.0} L_{\odot}$, with the distinction between LIRGs and ULIRGs being an artificial boundary in luminosity. Merging galaxies may alternate between luminous and ultraluminous states with some non-trivial duty cycle. The problem reduces to one of luminosity evolution during the merging process. Clearly ULIRGs pass through the “luminous” state during their normal course of development. Figure 21 depicts an example scenario of luminosity evolution for a major merger. This diagram is merely suggestive, but roughly speaking, is capable of reproducing luminosity functions for luminous infrared galaxies, as well as integrated gas depletion via star formation.

The companion, non-active galaxies in the ULIRGs

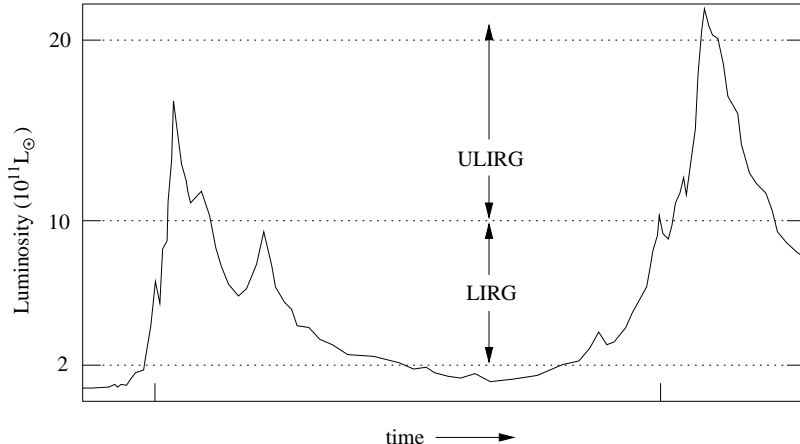


FIG. 21.— Cartoon representation of a possible luminosity evolutionary sequence as a function of time during the merger process. This particular example shows three principal peaks in luminosity, corresponding to the two progenitor galaxies reacting to the first encounter, followed later by the burst corresponding to the final merger. In this representation, a significant portion of the merger lifetime is spent in the “luminous” phase, and the ultraluminous phases are much like islands poking above the luminosity floor. The ticks along the time axis signify the epochs of the first and final encounters. The fine structure in the light curve is simply intended to indicate that critical processes associated with rates at which fuel is made available or can collapse into stars may vary on timescales of a few million years or less.

seen in this sample provide *in situ* examples of what the ULIRGs might look like in the non-ultraluminous state. Just as observed for LIRGs, these galaxies host extended star formation across large portions of their disks. With moderate star formation rates of a few $\times 10 M_{\odot} \text{ yr}^{-1}$, these galaxies may still preserve enough fuel supply for a final burst, yet have enough activity to classify as LIRGs for a substantial fraction of the encounter duration.

Indeed LIRGs are frequently found in merging pairs, with the fraction of LIRGs classified as strongly interacting rising from 40% at the lower luminosity cutoff to $\sim 100\%$ at the high end (Sanders 1992). LIRGs are more abundant than ULIRGs in a given volume of space by at least a factor of 20–30 (Soifer et al. 1987). If $\sim 60\%$ of LIRGs are associated with major mergers, then there are at least ten times as many major mergers classified as LIRGs than as ULIRGs. If indeed these two classes of galaxies represent different phases of the same phenomenon, then the ultraluminous duty cycle would be around 10% of the luminous phase in galactic encounters between massive, gas-rich galaxies. For the discussion to follow, only the LIRGs identified with strong interactions are considered in comparison to ULIRGs.

Obviously this connection between LIRGs and ULIRGs is an oversimplification. Surely some LIRGs will never reach ultraluminous status due to the lack of raw materials. Yet CO measurements in interacting LIRGs and ULIRGs in similar merger states (double nucleus systems with overlapping disks) presented by Gao & Solomon (1999) indicate that LIRGs have similar amounts of molecular gas compared to ULIRGs, with median CO luminosities of 5.8×10^9 and 9.0×10^9 respectively, in units of $\text{K km s}^{-1} \text{ pc}^{-2}$. Yet the median infrared luminosities of the LIRGs and ULIRGs in their sample differ by a factor of four. Moreover, carefully examining the Gao & Solomon data, one finds no dramatic trend of CO luminosity with L_{ir} across the LIRG sample. Therefore, it seems that interacting LIRGs and ULIRGs share similar quantities of molecular gas. Under the conservative assumption that only half of the LIRGs have quantities of molecular gas

similar to that found in ULIRGs, the estimated ultraluminous duty cycle changes from 10% to 20% based on relative number densities. The estimates of duty cycles in this way are consistent with the duty cycles estimated from comparing timescales of mergers and ultraluminous starbursts.

A preliminary characterization of the morphological properties of strongly interacting LIRGs in the Revised Bright Galaxy Sample (RBGS) (Mazzarella et al. 2001) indicates that the proposed ULIRG-LIRG evolutionary connection does hold some merit. If LIRGs were simply weaker versions of ULIRGs, then they would be found in similar states of merging. Yet both the mean and median separations for double nucleus LIRGs in the RBGS are roughly twice that found in the 2 Jy ULIRG sample from Murphy et al. (1996). This applies for both samples as a whole, as well as for subsets containing only double galaxies. The range of nuclear separations observed is the same in both the LIRG and ULIRG samples, including the zero-separation post-merger systems. These figures are summarized in Table 6. The ULIRGs in Table 6 are on average about four times more distant than the LIRGs, so that the absence of close-separation double LIRGs as compared to ULIRGs is a real and significant effect.

One argument against this evolutionary connection between ULIRGs and LIRGs is that LIRGs could simply represent weaker (i.e., larger impact parameter) galactic interactions. This would result in two observable consequences. First, weaker interactions would obviously produce less dramatic distortions in the way of tidal tails and warped isophotes. No immediate difference in these morphological features is apparent in the imaging data. Second, wider approaches would be less affected by dynamical friction, resulting in much larger apocentric distances for the weaker interactions. The observed range in separations among LIRGs and ULIRGs is almost identical, so that both consequences of weaker interactions are not directly reflected in the imaging data.

The same early/late age classification that was performed on the 2 Jy ULIRG sample was also performed on

the RBGS LIRGs, the histogram for which is presented in Figure 19 along with the ULIRG data. The age distributions of LIRGs are subtly different from that of ULIRGs, in that the estimated LIRG ages do not cluster so tightly around the times of the initial and final encounters. Put in the context of luminosity evolution, the age classification data are consistent with the notion that LIRGs represent the tail of the first-encounter ULIRG burst, and also appear as a precursor to the final merger. It should be pointed out that the post-merger LIRGs and ULIRGs are placed into the last three bins of the histograms in Figure 19. In reality, there could be a radical difference in the age distribution for post-merger LIRGs and ULIRGs. ULIRGs are still confined temporally by the fact that they cannot produce ultraluminous power levels via starbursts for more than $\sim 10^8$ yr. LIRGs are not quite as restricted in this regard. Studying the morphologies of post-merger ULIRGs and LIRGs may be a way to probe the time since merger, based on the extent to which the system has relaxed from the violent process of coalescence. Such analysis is not attempted here. If the LIRGs are indeed found to exist at later post-merger times than ULIRGs, then just as with early bursts, these LIRGs could simply be the fading embers of ULIRGs.

5. CONCLUSIONS

Merging galactic systems are by their very nature complex, rapidly evolving entities. Integral field spectroscopy offers an ideal way in which to capture this complexity across the entire two-dimensional spatial extent. Often the added dimension of information allows one to reconstruct the full merger geometry. Among the more direct results of this work are the following findings:

1. Ultraluminous galaxies may be found at very early times in the merger sequence, perhaps $\lesssim 5 \times 10^7$ yr after the first close encounter.
2. Even the very early events seem to produce their ultraluminous emission from a highly concentrated nuclear starburst, in each case associated with the prograde nucleus.
3. There exists significant extinction to the nuclear line emission region, generally greater than 1 magnitude at $2 \mu\text{m}$. Thus a hidden AGN would be difficult to detect, even at these wavelengths.
4. Young tidal tails can host appreciable star formation at rates of several solar masses per year, perhaps related to the existence of crossing orbits during the early stages of tail formation.

5. ULIRGs may also be found at intermediate times, well after the first close encounter, and just prior to the final merger.
6. The observation that ULIRGs may be found at very young merger ages, together with the paucity of large-separation double ULIRGs, suggests an approximately bimodal time distribution of ultraluminous activity within the merger sequence. Most ULIRGs are seen just following the first major encounter or during the process of the final merger.

The surprising result that many ULIRGs appear to be quite young brings into question the nature of luminosity evolution for major galactic mergers. We suggest that many of the major galactic mergers currently seen in less luminous states have gone through or will eventually pass through an ultraluminous phase, depending on the efficiency and rapidity with which molecular gas can be funneled into the nuclear regions. Most ULIRGs seem to go through an ultraluminous state during the final merger, but some also experience early bursts. The early-bursting ULIRGs may be able to preserve enough fuel to sustain a second ultraluminous burst, or alternatively, the companion galaxy may supply the raw materials for this final event.

We are very grateful for the generosity of Joe Mazzarella, who allowed us to access the pre-publication images of the RBGS catalog. Eiichi Egami assisted with some of the observations. Ashish Mahabel graciously donated telescope time to acquire a J band image of IRAS 10190+1322. John Hibbard provided a thorough review, and many excellent suggestions, for which we are thankful. We acknowledge Michael Strauss for his role in the early study of the 2 Jy ULIRG sample. We also thank Gerry Neugebauer, Christopher Mihos, Andrew Baker, Lars Hernquist, and Andreas Eckart for helpful discussions. We thank the night assistants at Palomar, Rick Burruzz, and Karl Dunscombe for their assistance in the observations. This research has made use of the NASA/IPAC Extragalactic Database (NED), which is operated by the Jet Propulsion Laboratory, Caltech under contract with NASA. T.W.M. is supported by the NASA Graduate Student Researchers Program, and the Lewis Kingsley Foundation. This research is supported by a grant from the National Science Foundation.

APPENDIX

MERGER TIME CLASSIFICATION

The age of a merger, as determined from imaging data, is guided by two principles. The first is that tidal tails and related debris take time to grow to large scales. When the tidal extensions are much larger than the nuclear separation between galaxies, it may be assumed that the galaxy pair is seen well after the initial encounter. There is, of course, the possibility that multiple close encounters occur before the final coalescence of nuclei. The implicit assumption in this analysis is that only two encounters occur—an initial passage followed by a final merger. The very presence of tidal tails indicates a short-lived and intense disturbance in the not-so-distant past. Slow, spiraling approaches to merging would not produce these striking features, so that tidal tails imply moderately eccentric encounter orbits. Even collisionless

encounters drain energy and angular momentum from the core galaxies through dynamical friction and by throwing off tidal material to great distances. The detailed simulations of galaxy mergers (e.g., Mihos & Hernquist 1996; Barnes & Hernquist 1996) suggest that even previously unbound (or critically bound) galaxies with a 10 kpc first-encounter pericentric distance undergo a single subsequent large separation before plunging back together for the final merger. Thus any obvious and vastly extended tidal debris is assumed to have been generated in a previous close encounter, with the galaxies presently on the verge of permanently joining each other. Conversely, short, high-surface-brightness tidal tails are assumed to be recent formations, indicating a young encounter.

The second guiding morphological clue deals with the inner morphologies of the galaxies. Because the galaxies probably spend a few dynamical timescales between the time of first encounter and the final collision, the galaxies have a chance to reorganize themselves, ameliorating structural perturbations caused by the encounter. Thus highly distorted inner morphologies, such as obvious bar modes and warped disks likely indicate a young merger. Often, the warped features correspond to the stubby beginnings of a tidal tail.

Large scale tidal features take precedence over the more subjective assessment of distorted inner isophotes in assessing the age of the merger. The absence of apparent large scale tidal structures presents an ambiguity between their true absence or their low surface brightness. In these cases, either the presence of a short tail-like extension or obviously warped inner structure flags the ULIRG as an early merger. But without these additional clues, the age of the merger cannot be easily determined. This population is indicated in Figure 19 by the unshaded bins, and these bins are doubly represented at both early and late times.

Conversion of galaxy separation to time along the merger sequence is not performed in any sophisticated manner. The galaxies are simply assumed to experience a quadratic separation profile in time, i.e., constant acceleration. It is easy to justify this behavior when the galaxies are at apocenter, because at this time, the highly eccentric orbits are very nearly parabolic. As the distance between the galaxies diminishes, the acceleration would increase if the galaxies were point masses. But the vast dark matter halos of the galaxies act to soften the interaction. Representing the dominant mass component, the dark halos begin to overlap, resulting in a diminished net acceleration. These two effects roughly cancel each other, leading to a nearly parabolic time-separation relation. Numerical integration of halo mass interactions, using halo distribution functions like those detailed in Mihos & Hernquist (1996), show little departure from this behavior.

The parameters of the parabolic separation function are chosen to approximately represent the situation found in ULIRGs. The maximum separation observed in the 2 Jy ULIRG sample is 48 kpc (Murphy et al. 1996), so we will adopt 50 kpc as the nominal maximum separation for each encounter. If the timescale for the encounter (initial close approach to second close approach) is 10^9 yr, the maximum relative velocity will be 200 km s^{-1} , closely matching observed velocity differences in close pairs (Murphy et al. 2001). The exact mapping function used to convert the projected separations in Table 5 to time along the merger sequence is

$$\Delta r = \left[50 - 2 \left(\frac{t}{10^8 \text{ yr}} - 5 \right)^2 \right] \text{ kpc},$$

inverting to

$$t = \left(5 \pm \sqrt{\frac{50 - \left(\frac{\Delta r}{1 \text{ kpc}} \right)}{2}} \right) \times 10^8 \text{ yr},$$

where the plus sign is used for late stage mergers, and the minus sign for early stage mergers. The resulting time stretch has the dramatic effect of putting virtually all observed ULIRGs at either very early or very late times. A few objects appear at intermediate times, demonstrating that the ultraluminous phenomenon can be rather delayed. But by-and-large, the ULIRG temporal distribution appears to be bimodal.

Table 5 presents the somewhat subjective age classifications for the double nucleus galaxies in the complete 2 Jy sample, as defined in Murphy et al. (1996). Most of the classifications are based on the images found in Murphy et al., though supplemental data were obtained from Surace et al. (1998) and Surace, Sanders, & Evans (2000). Note the tendency for the galaxies classified as early interactions to have luminosities at the low end of the ultraluminous range. This is displayed graphically in Figure 20, and suggests that this scheme of classification is less than random.

REFERENCES

Armus, L., Heckman, T. M., & Miley, G. K. 1990, *ApJ*, 364, 471
 Barnes, J. E., & Hernquist, L. 1992, *Nature*, 360, 715
 Barnes, J. E., & Hernquist, L. 1996, *ApJ*, 471, 115
 Barton, E. J., Geller, M. J., Bromley, B. C., van Zee, L., & Kenyon, S. J. 2001, *AJ*, 121, 625
 Carico, D. P., Graham, J. R., Matthews, K., Wilson, T. D., Soifer, B. T., Neugebauer, G., & Sanders, D. B. 1990, *ApJ*, 349, L39
 Chrome, F. R., Elmegreen, D. M., Mandell, A., & McDermott, J. 1998, *AJ*, 115, 2331
 Clements, D. L., Sutherland, W. J., McMahon, R. G., & Saunders, W. 1996, *MNRAS*, 279, 477
 Crawford, T., Marr, J., Partridge, B., & Strauss, M. A. 1996, *ApJ*, 460, 225
 Downes, D., Solomon, P. M., & Radford, S. J. E. 1993, *ApJ*, 414, L13
 Duc, P.-A., & Mirabel, I. F. 1998, *A&A*, 333, 813
 Duc, P.-A., et al. 2000, *AJ*, submitted
 Elmegreen, B. G., Kaufman, M., & Thomasson, M. 1993, *ApJ*, 412, 90
 Gao, Y., & Solomon, P. M. 1999, *ApJ*, 512, L99
 Goldader, J. D., Joseph, R. D., Doyon, R., & Sanders, D. B. 1995, *ApJ*, 444, 97
 Hibbard, J. E., & van Gorkom, J. H. 1996, *AJ*, 111, 655

Higdon, J. L. 1995, *ApJ*, 455, 524
 Higdon, J. L., & Wallin, J. F. 1997, *ApJ*, 474, 686
 Higdon, J. L., Rand, R. J., & Lord, S. D. 1997, *ApJ*, 489, L133
 Hunter, D. A., Gillett, F. C., Gallagher, J. S., Rice, W. L., & Low, F. J. 1986, *ApJ*, 303, 171
 Inoue, A. K., Hirashita, H., & Kamaya, H. 2000, *PASJ*, in press (astro-ph/0003318)
 Larkin, J. E., Knop, R. A., Lin, S., Matthews, K., & Soifer, B. T. 1996, *PASP*, 108, 211
 Kennicutt, R. C. 1983, *ApJ*, 272, 54
 Kim, D.-C., Veilleux, S., & Sanders, D. B. 1998, *ApJ*, 508, 627
 Mazzarella, J. M., Sanders, D. B., Kim, D. -C., & Jenson, J. B. 2001, in preparation
 Mihos, J. C., & Hernquist, L. 1996, *ApJ*, 464, 641
 Mihos, J. C., & Bothun, G. D. 1997, *ApJ*, 481, 741
 Mihos, J. C., & Bothun, G. D. 1998, *ApJ*, 500, 619
 Mirabel, I. F., Dottori, H., & Lutz, D. 1992, *A&A*, 256, L19
 Murphy, T.W., Armus, L., Matthews, K., Soifer, B. T., Mazzarella, J. M., Shupe, D. L., Strauss, M. A., & Neugebauer, G. 1996, *AJ*, 111, 1025
 Murphy, T. W., Matthews, K., and Soifer, B. T. 1999, *PASP*, 111, 1176
 Murphy, T. W., Soifer, B. T., Matthews, K., Kiger, J. R., & Armus, L. 1999, *ApJ*, 525, L85
 Murphy, T. W. Jr. 2000, Ph.D. thesis, California Institute of Technology
 Murphy, T.W., Soifer, B. T., Matthews, K., Armus, L., & Kiger, J. K. 2001, *AJ*, 121, 97
 Noguchi, M. 1991, *MNRAS*, 251, 360
 Oke, J. B., & Gunn, J. E. 1983, *ApJ*, 266, 713
 Osterbrock, D. E. 1989, *Astrophysics of Gaseous Nebulae and Active Galactic Nuclei* (Mill Valley, CA: University Science)
 Persson, S. E., Murphy, D. C., Krzemenski, W., Roth, M., & Rieke, M. J. 1998, *AJ*, 116, 2475
 Pierce, M. J., & Tully, R. B. 1992, *ApJ*, 387, 47
 Reshetnikov, V. P. 1998, *Astronomy Letters*, 24, 153
 Rieke, G. H., & Lebofsky, M. J. 1985, *ApJ*, 288, 618
 Sakamoto, K., Scoville, N. Z., Yun, M. S., Crosas, M., Genzel, R., & Tacconi, L. J. 1999, *ApJ*, 514, 68
 Sanders, D. B., Soifer, B. T., Elias, J. H., Madore, B. F., Matthews, K., Neugebauer, G., & Scoville, N. Z. 1988, *ApJ*, 325, 74
 Sanders, D. B., Scoville, N. Z., & Soifer, B. T. 1991, *ApJ*, 370, 158
 Sanders, D. B. 1992, in *ASP Conference Series*, Vol. 31, Relationships between Active Galactic Nuclei and Starburst Galaxies, ed. A. Filippenko (San Francisco: ASP), 303
 Sanders, D. B., & Mirabel, I. F. 1996, *ARA&A*, 34, 749
 Schlegel, D. J., Finkbeiner, D. P., & Davis, M. 1998, *ApJ*, 500, 525
 Schweizer, F. 1978, in *IAU Symposium 77, The Structure and Properties of Nearby Galaxies*, ed. E. M. Berkhuijsen & R. Wielebinski (Dordrecht: Reidel), 279
 Scoville, N. Z., & Young, J. S. 1983, *ApJ*, 265, 148
 Soifer, B. T., Neugebauer, G., Matthews, K., Egami, E., Becklin, E. E., Weinberger, A. J., et al. 2000, *AJ*, 119, 509
 Soifer, B. T., Sanders, D. B., Madore, B. F., Neugebauer, G., Danielson, G. E., et al. 1987, *ApJ*, 320, 238
 Solomon, P. M., Downes, D., Radford, S. J. E., & Barrett, J. W. 1997, *ApJ*, 478, 144
 Strauss, M. A., Davis, M., Yahil, A., & Huchra, J. P. 1990, *ApJ*, 361, 49
 Strauss, M. A., Huchra, J. P., Davis, M., Yahil, A., Fisher, K. B., & Tonry, J. 1992, *ApJS*, 83, 29
 Strauss, M. A. 1993, private communication
 Surace, J. A., Sanders, D. B., Vacca, W. D., Veilleux, S., & Mazzarella, J. M. 1998, *ApJ*, 492, 116
 Surace, J. A., Sanders, D. B., & Evans, A. S. 2000, *ApJ*, 529, 170
 Toomre, A., & Toomre, J. 1972, *ApJ*, 178, 623
 Trung, D.-V., Lo, K. Y., Kim, D.-C., Gao, Y., & Gruendl, R. A. 2001, astro-ph/0103285
 Tyson, J. T., Fischer, P., Guhathakurta, P., McIlroy, P. et al. 1998, *AJ*, 116, 102
 Veilleux, S., Kim, D.-C., & Sanders, D. B. 1999 *ApJ*, 522, 113
 Wallin, J. F. 1990, *AJ*, 100, 1477
 Zwicky, F. 1956, *Ergebnisse der Exakten Naturwissenschaften*, 29, 344

TABLE 1
ULIRG SAMPLE

Galaxy	Morphological ^a Classification	cz ^b (km s ⁻¹)	$\log \frac{L_{ir}}{L_{\odot}}$ ^c	physical scale ^c (kpc arcsec ⁻¹)
IRAS 01521+5224	double	23931	11.95	1.38
IRAS 10190+1322	double	22867	11.98	1.33
IRAS 17574+0629	single ?	32701	12.10	1.82
IRAS 20046-0623	single ?	25219	12.02	1.45

^aBased on K_s band morphology

^bMeasured from this dataset at the position of the continuum peak coinciding with the strongest Pa α emission

^cAssumes $H_0 = 75$ km s⁻¹, and $q_0 = 0$

TABLE 2
INTEGRAL FIELD OBSERVATIONS

Galaxy	Date	Integration Time	Seeing	P.A.	$\lambda_{Pa\alpha}$ (μ m)
IRAS 01521+5224S	15 November 1999	3600 s	0''8	87°	2.0248
IRAS 01521+5224N	15 November 1999	2400 s	0''8	87°	2.0248
IRAS 10190+1322	24 March 1999	2400 s	0''8	65°	2.0189
IRAS 17574+0629	24 July 1999	2400 s	0''9	51°	2.0806
IRAS 20046-0623	25 July 1999	1200 s	0''75	90°	2.0337

TABLE 3
INFRARED IMAGING OBSERVATIONS

Galaxy	Date	K_s Exposures \times Integration Time	Seeing
IRAS 01521+5224	25 November 1996	4 \times 20 s	0''8
IRAS 10190+1322	22 May 1997	4 \times 10 s	0''.75
IRAS 17574+0629	3 August 1996	6 \times 30 s	0''.7
IRAS 20046-0623	3 August 1993	8 \times 20 s	0''.9

TABLE 4
VISUAL OBSERVATIONS

Galaxy	Date	r Exposures \times Integration Time	$H\alpha$ Exposures \times Integration Time	Seeing
IRAS 01521+5224	21 January 1996	2 \times 600 s	2 \times 900 s	1''.5
IRAS 10190+1322	9 December 1996	1 \times 300 s	...	2''.3
IRAS 17574+0629	3 June 1994	1 \times 600 s	1 \times 900 s	1''.2
IRAS 20046-0623	7 November 1993	2 \times 600 s	3 \times 900 s	1''.5

TABLE 5
MERGER AGE CLASSIFICATION

Galaxy	Separation ^a (kpc)	$\log \frac{L_{ir}}{L_{\odot}}$	Age Category	Comments
IRAS 00153+5454	8.1	12.10	early	distorted disks, confined debris
IRAS 01521+5224 ^b	7.7	11.95	early	short, bright tails, distorted
IRAS 05246+0103	9.6	12.05	early	distorted, short tail?
IRAS 09061-1248	6.4	11.97	early	distorted disks, confined debris
IRAS 09111-1007	36.0	11.98	early	distortion, bars?—both disks
IRAS 09583+4714	13.0	11.98	early	distortion, bars—both disks
IRAS 10035+4852	11.4	11.93	early	two bright, relatively short tails
IRAS 10565+2448	20.2	11.98	early	tail length similar to separation
IRAS 14348-1447	4.8	12.28	early	short, bright tail
IRAS 14394+5332	48.0	12.04	early	near apogee—early/late irrelevant
IRAS 16474+3430	6.5	12.12	early	short, bright tail, distorted
IRAS 17028+5817	22.5	12.11	early	distorted, short tidal features
IRAS 18470+3233	9.4	12.02	early	two very distorted disks
IRAS 20046-0623 ^b	3.6	12.02	early	short, bright tail
IRAS 23327+2913	21.7	12.03	early	distorted, young bridge/tail
IRAS 00091-0738	2.3	12.21	late	tidal debris much larger than sep.
IRAS 00188-0856	14.1	12.33	late	symmetric, no bright tidal extensions
IRAS 03158+4227	40.0	12.55	late	both symmetric
IRAS 03521+0028	3.6	12.48	late	large, diffuse tidal features
IRAS 10190+1322 ^b	5.3	11.98	late	symmetric, no bright tidal extensions
IRAS 12071-0444	1.8	12.31	late	tidal tail much larger than separation
IRAS 12112+0305	3.7	12.27	late	mature tidal features
IRAS 12540+5708	2.8	12.50	late	large scale tidal debris
IRAS 13451+1232	3.9	12.27	late	symmetric, large scale tidal debris
IRAS 15245+1019	3.4	11.96	late	large scale tidal tail
IRAS 21396+3623	15.4 ^c	12.40 ^c	late	symmetric, no bright tidal extensions
IRAS 22491-1808	2.1	12.12	late	large, diffuse tidal features
IRAS 08572+3915	5.8	12.08	unknown	ambiguous tidal structure
IRAS 13539+2920	7.2	12.04	unknown	some distortion, could be early
IRAS 16487+5447	5.3	12.12	unknown	diffuse tidal fuzz, could be late

^aProjected separation is converted into merger age via the quadratic formulation described in Appendix A.

^bMember of the present sample

^cRevised redshift from Strauss et al. (1992) value: $cz = 44750 \text{ km s}^{-1}$

TABLE 6
LIRG AND ULIRG SEPARATIONS

Sample	Number	Mean Separation (kpc)	Median Separation (kpc)	Separation Range (kpc)	Mean L_{ir} ($10^x L_{\odot}$)
LIRGs: all	51	10.3	4.9		11.54
doubles	28	18.7	12.3	3.6-49	11.55
ULIRGs: all	64	5.4	0.15		12.16
doubles	32	10.8	6.4	0.3-48	12.13

Note. — The median ULIRG separation is reported as 0.15 kpc—a consequence of exactly half of the sample being measured doubles, with the minimum separation double ULIRG being Arp 220, at 0.3 kpc projected separation.